

# Estimation of the XUV radiation onto close planets and their evaporation

J. Sanz-Forcada<sup>1</sup>, G. Micela<sup>2</sup>, I. Ribas<sup>3</sup>, A. M. T. Pollock<sup>4</sup>, C. Eiroa<sup>5</sup>, A. Velasco<sup>1,6</sup>, E. Solano<sup>1,6</sup>, and D. García-Álvarez<sup>7,8</sup>

<sup>1</sup> Departamento de Astrofísica, Centro de Astrobiología (CSIC-INTA), ESAC Campus, P.O. Box 78, E-28691 Villanueva de la Cañada, Madrid, Spain;

e-mail: jsanz@cab.inta-csic.es

<sup>2</sup> INAF – Osservatorio Astronomico di Palermo G. S. Vaiana, Piazza del Parlamento, 1; Palermo, I-90134, Italy

<sup>3</sup> Institut de Ciències de l’Espai (CSIC-IEEC), Campus UAB, Fac. de Ciències, Torre C5-parell-2<sup>a</sup> planta, E-08193 Bellaterra, Spain

<sup>4</sup> XMM-Newton SOC, European Space Agency, ESAC, Apartado 78, E-28691 Villanueva de la Cañada, Madrid, Spain

<sup>5</sup> Dpto. de Física Teórica, C-XI, Facultad de Ciencias, Universidad Autónoma de Madrid, Cantoblanco, E-28049 Madrid, Spain

<sup>6</sup> Spanish Virtual Observatory, Centro de Astrobiología (CSIC-INTA), ESAC Campus, Madrid, Spain

<sup>7</sup> Instituto de Astrofísica de Canarias, E-38205 La Laguna, Spain

<sup>8</sup> Grantecan CALP, E-38712 Breña Baja, La Palma, Spain

Received ; accepted

## ABSTRACT

**Context.** The current distribution of planet mass vs. incident stellar X-ray flux supports the idea that photoevaporation of the atmosphere may take place in close-in planets. Integrated effects have to be accounted for. A proper calculation of the mass loss rate due to photoevaporation requires to estimate the total irradiation from the whole XUV range.

**Aims.** The purpose of this paper is to extend the analysis of the photoevaporation in planetary atmospheres from the accessible X-rays to the mostly unobserved EUV range by using the coronal models of stars to calculate the EUV contribution to the stellar spectra. The mass evolution of planets can be traced assuming that thermal losses dominate the mass loss of their atmospheres.

**Methods.** We determine coronal models for 82 stars with exoplanets that have X-ray observations available. Then a synthetic spectrum is produced for the whole XUV range ( $\sim 1 - 912$  Å). The determination of the EUV stellar flux, calibrated with real EUV data, allows us to calculate the accumulated effects of the XUV irradiation on the planet atmosphere with time, as well as the mass evolution for planets with known density.

**Results.** We calibrate for the first time a relation of the EUV luminosity with stellar age valid for late-type stars. In a sample of 109 exoplanets, few planets with masses larger than  $\sim 1.5 M_J$  receive high XUV flux, suggesting that intense photoevaporation takes place in a short period of time, as previously found in X-rays. The scenario is also consistent with the observed distribution of planet masses with density. The accumulated effects of photoevaporation over time indicate that HD 209458b may have lost  $0.2 M_J$  since an age of 20 Myr.

**Conclusions.** Coronal radiation produces rapid photoevaporation of the atmospheres of planets close to young late-type stars. More complex models are needed to explain fully the observations. Spectral energy distributions in the XUV range are made available for stars in the sample through the Virtual Observatory, for the use in future planet atmospheric models.

**Key words.** (stars:) planetary systems – stars: coronae – astrobiology – x-rays: stars

## 1. Introduction

After 15 years of exoplanetary science, the discipline has reached a point at which it is possible to study in more detail the physical properties of planets, their formation and evolution. With more than 500 exoplanets known to date it is possible to explore relations between the planets and their host stars. In particular, the mass of the planets and the atmospheric conditions are partly linked to the stellar radiation. Once the planet is formed, and the original disc is dissipated, the main agent interacting with the atmosphere should be the high energy emission from the corona of the star, for late type stars (Lammer et al., 2003; Erkaev et al., 2007; Penz et al., 2008; Cecchi-Pestellini et al., 2009, Sanz-Forcada et al. 2010b, and references therein). Recently Sanz-Forcada et al. (2010b), (hereafter Paper I) noticed that erosion in exoplanets may be taking place as an effect of coronal radiation vaporizing the atmosphere of close-in planets: they showed that distribution of

planet masses with the X-ray flux at the planet implies that the least massive planets currently receive a high X-ray flux. This is interpreted as the effect of radiation erosion in the long term.

Photons with  $\lambda < 912$  Å can ionize hydrogen atoms, assumed to be the main component of the atmosphere of giant planets. The effects of X-rays ( $\lambda\lambda$  5–100) and Extreme Ultraviolet (EUV,  $\lambda\lambda$  100–912) photons take place at different heights in the atmosphere of the planet. While EUV photons mainly ionize the atoms in the upper atmosphere, X-rays penetrate deeper into the atmosphere. The free electrons carry a high momentum, producing a cascade of collisions while the X-rays photons are absorbed in the atmosphere (Cecchi-Pestellini et al., 2009). These collisions heat the atmosphere yielding its “inflation” and eventually the evaporation of a part of it. The gravity of the planet acts as protection, trying to keep the atmosphere attached to the planet. If we assume that the planet atmosphere is mainly composed of hydrogen, and all the photons

in the whole XUV range (X-rays+EUV) are absorbed and contribute to the heating of the atmosphere, it is possible to calculate the mass loss of the atmosphere by balancing the losses with the planet gravity (Watson et al., 1981; Lammer et al., 2003). An additional source of mass loss takes place through the Roche Lobe for close-in planets (Erkaev et al., 2007) (see also Lecavelier des Etangs et al., 2004; Jaritz et al., 2005, for detailed simulations of the escape through Roche Lobe). The resulting formula (Paper I) is:

$$\dot{M} = \frac{\pi R_p^3 F_{\text{XUV}}}{G K M_p} \quad (1)$$

where  $K$  ( $K \leq 1$ ) accounts for the planet radius Roche Lobe losses (Erkaev et al., 2007),  $F_{\text{XUV}}$  is the X-ray and EUV flux at the planet orbit, and  $G$  is the gravitational constant<sup>1</sup>. Baraffe et al. (2004) consider that evaporation actually takes place at a point somewhere above the planet radius  $R_p$ , at the “expansion radius”  $R_1$ . However the bulk of the XUV radiation should be absorbed by material enclosed within the planet radius, so we assume that  $R_1 \approx R_p$ . The formula can be simplified using the mean density of the planet ( $\rho$ ), and assuming that  $K \approx 1$  (valid for most cases, and a lower limit to the mass loss in any case):

$$\dot{M} = \frac{3 F_{\text{XUV}}}{4 G \rho} \quad (2)$$

Stars in the range late-F to mid-M stellar types are characterized by coronae with temperatures of  $\sim 1$  MK, exceeding 10 MK in the most active cases. The high temperature material in the transition region ( $\sim \log T = 4 - 5.8$ ) and corona ( $\sim \log T = 5.8 - 7.4$ ) emits copious X-rays and EUV flux. Fast rotators have hotter coronae, resulting in higher XUV fluxes. Current astronomical instruments give access to the X-rays band only. More energetic flux ( $\lambda \lesssim 1$  Å) is negligible even for active stars, while the radiation in the EUV band is severely absorbed by the neutral and molecular hydrogen in the interstellar medium (ISM). There are no missions currently observing in the EUV band, and the few data from past telescopes, such as EUVE (Extreme Ultraviolet Explorer), are limited to the closest stars in the range  $\lambda 100 - 400$ . Only one star hosting an exoplanet has been observed in this band,  $\epsilon$  Eri (Sanz-Forcada et al., 2003a).

The present-day distribution of planet masses should reflect the accumulated effects of mass loss in the atmospheres of the planet over time (Paper I). Moreover, if we know the evolution of the emission in the whole XUV band we should be able to trace the planet evolution, given an accurate knowledge of the density of the planet, according to Eq. 2. Since younger stars have faster rotation, their coronae emit more XUV flux, which therefore decreases with time. The evolution of the X-ray emission with age has been studied for the Sun (e.g. Maggio et al., 1987; Ayres, 1997; Ribas et al., 2005) and extended to G and M stars (Penz & Micela, 2008; Penz et al., 2008). A relation using late F to early M stars has been calibrated by Garcés et al. (in preparation) in the X-ray band, allowing us to calculate the age of the stars from its X-ray emission (Paper I), and to trace the time evolution of this emission. In the EUV band the time evolution of the emission has been only studied for the Sun (Ribas et al., 2005).

<sup>1</sup> A factor of 4, used in Penz et al. (2008) and Paper I, has been removed to account for geometrical considerations, as explained in Eq. 21 of Erkaev et al. (2007)

**Table 1.** Observation log of stars with exoplanets<sup>a</sup>

Star name	Measured coordinates $\alpha, \delta$ (J2000.0)		Date	Instr. <sup>a</sup>	t (ks)	S/N	Notes
14 Her	16:10:24.6	+43:49:01	2005/09/11	EPIC	5	4.9	
16 Cyg B	19:41:48.9	+50:31:28	2008/11/08	EPIC	11	2.0	
2M1207 A	12:07:33.5	-39:32:54	2003/03/03	ACIS	50	0.4	
30 Ari B	02:36:57.6	+24:38:52	2001/01/16	EPIC	20	244	
			2001/01/17	EPIC	34		
47 UMa	10:59:28.4	+40:25:46	2006/06/11	EPIC	8	4.8	
51 Peg	22:57:28.1	+20:46:08	2008/12/06	ACIS	5	2.6	
55 Cnc	08:52:35.7	+28:19:47	2009/04/11	EPIC	12	14.0	
$\beta$ Pic	05:47:17.1	-51:03:59	2004/01/04	EPIC	68	5.7	
$\epsilon$ Eri	03:32:55.9	-09:27:31	2003/01/19	EPIC	12	297	
GJ 86	02:10:28.1	-50:49:19	2008/06/10	EPIC	15	43.0	WD in field
GJ 317	08:40:59.0	-23:27:15	2009/04/20	EPIC	18	9.6	
GJ 436	11:42:11.6	+26:42:16	2008/12/10	EPIC	30	14.5	
GJ 674	17:28:40.3	-46:53:50	2008/09/05	EPIC	44	179	
GJ 876	22:53:17.3	-14:15:55	2008/11/14	EPIC	23	34.7	
GQ Lup	15:49:12.1	-35:39:05	2008/08/16	EPIC	8	31.7	
HD 4308	00:44:39.4	-65:39:05	2008/12/02	EPIC	9	2.5	
HD 20367	03:17:40.1	+31:07:37	2005/02/11	EPIC	10	140	
HD 27442	04:16:29.0	-59:18:09	2009/02/10	EPIC	7	2.7	
HD 46375	06:33:12.4	+05:27:49	2005/10/14	EPIC	8	7.3	
HD 49674	06:51:30.9	+40:52:03	2006/04/10	EPIC	8	6.5	
HD 50554	06:54:42.8	+24:14:43	2006/04/16	EPIC	9	2.7	
HD 52265	07:00:18.0	-05:22:01	2008/09/19	EPIC	9	5.4	
HD 70642	08:21:28.2	-39:42:18	2006/04/08	EPIC	13	4.2	
HD 75289	08:47:40.1	-41:44:14	2005/04/28	EPIC	8	2.3	
HD 93083	10:44:20.9	-33:34:38	2008/05/26	EPIC	12	6.3	
HD 95089	10:58:47.7	+01:43:44	2009/05/26	EPIC	37	0.8	
HD 99492	11:26:45.9	+03:00:24	2008/06/19	EPIC	24	11.3	
HD 101930	11:43:30.1	-58:00:21	2009/01/06	EPIC	2	0.4	
HD 102195	11:45:42.2	+02:49:16	2008/06/15	EPIC	18	53.1	
HD 108147	12:25:46.2	-64:01:20	2002/08/10	EPIC	6	4.2	
HD 111232	12:48:51.8	-68:25:29	2008/07/29	EPIC	9	0.9	
HD 114386	13:10:39.7	-35:03:20	2008/07/29	EPIC	9	3.0	
HD 114762	13:12:19.7	+17:31:02	2004/06/28	EPIC	29	1.4	dM in field
HD 114783	13:12:43.7	-02:15:54	2009/01/22	EPIC	8	3.0	
HD 130322	14:47:32.8	-00:16:54	2005/07/21	EPIC	7	7.7	
HD 154345	17:02:36.5	+47:05:02	2008/12/25	EPIC	8	9.0	
HD 164922	18:02:33.4	+26:18:43	2009/03/19	EPIC	9	1.0	
HD 179949	19:15:33.3	-24:10:46	2005/05/21	ACIS	30	101	
			2005/05/22	ACIS	30		
			2005/05/29	ACIS	30		
			2005/05/30	ACIS	32		
			2005/05/31	ACIS	30		
HD 187123	19:46:57.9	+34:25:09	2006/04/21	EPIC	16	1.4	
HD 189733	20:00:43.8	+22:42:34	2007/04/17	EPIC	43	92.5	
HD 190360	20:03:37.9	+29:53:45	2005/04/25	EPIC	4	1.4	
HD 195019	20:28:18.6	+18:46:10	2006/04/24	EPIC	10	2.7	dK in field
HD 209458	22:03:10.8	+18:53:03	2006/11/15	EPIC	31	1.8	
HD 216435	22:53:38.1	-48:35:55	2006/04/21	EPIC	7	11.9	
HD 216437	22:54:39.6	-70:04:26	2005/04/13	EPIC	6	4.0	
HD 217107	22:58:15.7	-02:23:43	2005/05/16	EPIC	7	2.3	
HD 218566	23:09:10.9	-02:15:39	2001/06/10	EPIC	3	6.8	
			2004/06/05	EPIC	10		
HD 330075	15:49:37.7	-49:57:48	2005/08/07	EPIC	16	3.1	
HR 8799	23:07:28.8	+21:08:02	2009/08/30	ACIS	10	6.5	
$\mu$ Ara	17:44:08.7	-51:50:04	2008/09/06	EPIC	6	2.9	
			2008/10/02	EPIC	9		
NGC 2423 3	07:37:09.2	-13:54:24	2008/05/05	EPIC	9	1.1	
Pollux	07:45:18.8	+28:01:33	2001/04/26	EPIC	32	34.0	
$\tau$ Boo	13:47:15.9	+17:27:22	2003/06/24	EPIC	56	317	dM2 in field
$\nu$ And	01:36:47.7	+41:24:15	2009/10/20	ACIS	15	52.0	
			2009/10/22	ACIS	15		
			2009/10/27	ACIS	14		
			2009/10/29	ACIS	14		

**Notes.** <sup>(a)</sup> XMM-Newton (EPIC) or Chandra (ACIS) instrument used to measure the X-ray flux.

In this work we extend the analysis of Paper I to the EUV band, to account for all the stellar radiation capable to ionize hydrogen in a planet atmosphere. Lecavelier Des Etangs (2007) extrapolated the EUV flux from the X-ray flux, using the Sun as pattern for all kind of stars, without checking whether the relation is valid at all levels of activity, and therefore ages. Since there are essentially no measurements in the range  $\sim 400-912$  Å for stars other than the Sun, we use coronal models to synthesize

**Table 2.** ROSAT/SPPC X-ray flux (0.12–2.48 keV) of stars with exoplanets

Star name	Coordinates $\alpha, \delta$ (J2000.0)	S/N	$\log f_X$ ( $\text{erg s}^{-1}\text{cm}^{-2}$ )	Notes
18 Del	20:58:25.9 +10:50:21	4.5	-12.48	
1RXS 1609	16:09:30.3 -21:04:58	3.5	-12.52	
4 UMa	08:40:12.8 +64:19:40	11.6	-13.26	K-M in field
61 Vir	13:18:24.3 -18:18:40	5.7	-13.06	
$\alpha$ Ari	02:07:10.4 +23:27:44	5.1	-13.50	
BD-10 3166	10:58:28.8 -10:46:13	3.1	< -12.52	+dM5, uncertain <i>d</i>
$\gamma$ Cep	23:39:20.8 +77:37:56	8.1	< -13.03	dM4 in field
GJ 176	04:42:55.8 +18:57:29	3.2	-12.62	
GJ 832	21:33:34.0 -49:00:32	7.3	-12.69	
GJ 3021	00:16:12.7 -79:51:04	7.8	< -11.62	dM4 in field
HD 3651	00:39:21.8 +21:15:01	4.5	-12.89	
HD 10647	01:42:29.3 -53:44:27	N/A	-12.24	
HD 38529	05:46:34.9 +01:10:05	5.3	-12.37	
HD 41004 A	05:59:49.6 -48:14:22	7.5	< -12.02	dM2 in field
HD 48265	06:40:01.7 -48:32:31	6.0	-12.43	
HD 70573	08:22:50.0 +01:51:33	4.0	-12.31	uncertain <i>d</i>
HD 87883	10:08:43.1 +34:14:32	N/A	-12.99	
HD 89744	10:22:10.6 +41:13:46	7.6	-13.17	
HD 102365	11:46:31.1 -40:30:01	4.8	-13.20	faint dM4 in field
HD 128311	14:36:00.6 +09:44:47	7.5	-12.04	
HD 142415	15:57:40.8 -60:12:00	5.0	-12.50	
HD 147513	16:24:01.3 -39:11:34	16.2	-11.40	
HD 150706	16:31:17.6 +79:47:23	12.0	-12.13	
HD 169830	18:27:49.5 -29:49:00	16.8	-12.94	
HD 176051	18:57:01.5 +32:54:06	7.2	< -12.27	F9V in field
HIP 75458	15:24:55.8 +58:57:57	3.5	-13.66	
HIP 79431	16:12:41.8 -18:52:31	3.6	-13.50	ROSAT/WGA detector
HR 810	02:42:33.5 -50:48:01	7.0	-11.67	

**Notes.** The star GJ 667C (M1V) was well detected with ROSAT/SPPC (S/N=7.1), but its X-ray emission is attributed to its companions GJ 667A (K3V) and GJ 667B (K5V), at 43".

the Spectral Energy Distribution in the whole EUV range, and test the results in X-rays and the lower wavelengths of the band (100–400 Å) for a few cases with EUV spectra available. We have set up a database (<http://sdc.cab.inta-csic.es/xexoplanets>), that is freely available (within the Spanish Virtual Observatory), “X-exoplanets”. The database includes synthetic SEDs in the range 1–1200 Å for all the stars listed in Table 1. Objects will be incorporated in the future as they are observed in X-rays.

The paper is structured as follows: Section 2 describes the observations, Sect. 3 extends the X-ray analysis to the EUV band; Sect. 4 show the results found for the sample, that are discussed in Sect. 5, to list the conclusions of the work in Sect. 6.

## 2. Observations

Data acquired with the X-ray telescopes XMM-Newton, Chandra and ROSAT have been used in this work (Tables 1, 2). XMM-Newton and Chandra data were fetched from their public archives, including data awarded to us as P.I. or co-I. (XMM prop. ID #020653, #020000, #055102). Data were reduced following standard procedures, removing time intervals affected by high background, likely produced by space weather events. The expected position of the targets were calculated using the coordinates and proper motions provided by SIMBAD. XMM-Newton/EPIC and Chandra/ACIS have spatial resolution of 6" and 2" respectively. The cleaned observations (Table 1) were used to extract the low-resolution spectra provided by XMM-Newton/EPIC and Chandra/ACIS ( $E/\Delta E=20-50$ ). The ISIS package (Houck & Denicola, 2000) and the Astrophysics Plasma Emission Database (APED, Smith et al., 2001) were used to fit the spectra with coronal models of 1 to 3 temperature components (Table 3), depending on the quality of the spec-

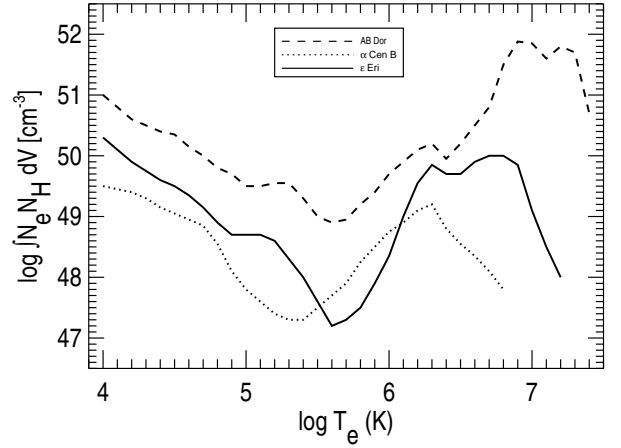


**Fig. 1.** Emission Measure Distribution (EMD) of three K2V stars with different levels of activity. The shape of solar EMD (Orlando et al., 2001) is similar to that of  $\alpha$  Cen B.

tra, and variable stellar coronal abundances, using the generally small value of the ISM absorption. The background spectrum was fitted simultaneously to the source to account for its contribution to the total spectrum. Spectra and light curves for each target are available on-line (<http://sdc.cab.inta-csic.es/xexoplanets>) in the “X-exoplanets” database (Sanz-Forcada et al., 2010a), described in detail in Appendix C. Spectra in the XUV range can be used for planet atmospheric models.

The spectra with lowest statistics have a deficient fit. This yields low abundance and very high emission measure, despite of the low temperature observed (emission measure in stellar coronae increase with the their coronal temperature). The use of solar abundance provides a similar fit, but with more realistic values of the emission measure. In these cases we fixed temperature and abundance to the solar values. We use  $\log T$  [K]=6.3 and the solar photospheric abundances of Asplund et al. (2005), corresponding to  $[\text{Fe}/\text{H}]=-0.2$  in the scale of Anders & Grevesse (1989) used in Table 3. The actual model used in the fit has little influence in the calculation of the X-ray (0.12–2.48 keV or  $\sim 5-100\text{\AA}$ ) flux displayed in Table 3, but it is important for the extension to the EUV range, as explained in Sect. 3. Table 3 lists also the errors for objects with net count rates with  $S/N>3$ , and consider the rest of detections as upper limits. We mark GJ 86 as an upper limit to account for the contribution of an unresolved companion.

ROSAT/SPPC observations were added to the sample. We consider only detections with  $S/N>3$ , given the lower spatial resolution of this instrument (25"), marking as upper limits objects with suspected X-ray bright companions, as indicated in Table 2 (as a reference, a dM3 star may have up to  $\log L_X \sim 27.5$ ). To calculate the X-ray flux of the targets we consider the count rate (CR) reported in HEASARC (<http://heasarc.gsfc.nasa.gov/>), corresponding to the spectral range 0.12–2.48 keV, and then transform it into flux using  $f_X = CR \times 6.19 \times 10^{-12} \text{ erg cm}^{-2} \text{ cts}^{-1}$ , as proposed by Schmitt et al. (1995) and Huensch et al. (1998), using a hardness ratio of -0.4 (corresponding to a middle activity level star,  $\epsilon$  Eri).

The stellar distance, not available for three ROSAT stars, was calculated using the spectroscopic parallax method, i.e., comparing the visual magnitude  $V$  with the absolute magnitude  $M_V$  that corresponds to the spectral type of the star (Cox, 2000). We cal-

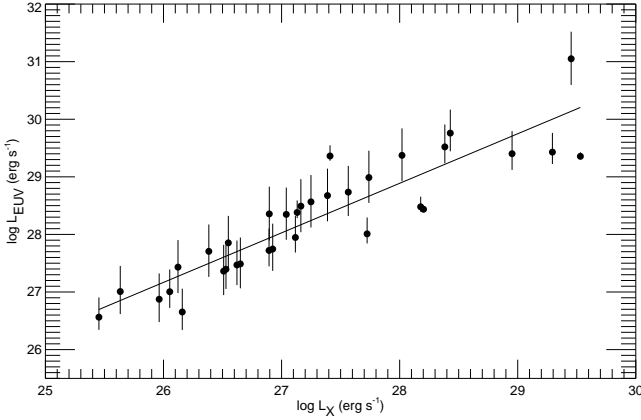


**Fig. 2.** X-ray vs EUV luminosity in selected stars of the sample (see text). Uncertainties come from calculation of the transition region EMD.

culated the bolometric luminosity ( $L_{\text{bol}}$ ) of each star using the bolometric corrections by Flower (1996) and B-V colors based on spectral types in Cox (2000) if no direct measurements are available in SIMBAD. The calculation of the age of the stars depends partly on  $L_{\text{bol}}$  (Paper I). We notice discrepancies with the  $L_{\text{bol}}$  calculated by Poppenhaeger et al. (2010) for some objects. The latter values are unrealistically high for GJ 832 (M1,  $\log L_{\text{bol}} [\text{erg s}^{-1}] = 35.86$ ), GJ 176/HD 285968 (M2V, 33.61), GJ 436 (M2, 33.52), HR 810 (G0V, 36.19), GJ 3021 (G6V, 36.02), HD 87833 (K0V, 34.37). These values correspond to spectral types of more massive stars. Finally some X-ray fluxes differ from other surveys (Kashyap et al., 2008; Poppenhaeger et al., 2010) mainly because they calculated the X-ray flux as a count rate conversion for most objects, or because of misidentifications of the stellar position in the field, as described in Paper I.

### 3. Extension to the EUV

In Paper I we calculated the X-ray fluxes that were received at the planet orbit ( $F_X$ ). We need to consider all the flux emitted by the star in the X-ray and EUV range in order to calculate the mass loss rate of the planet according to Eq. 2. Lecavelier Des Etangs (2007) extrapolated the EUV flux from the X-ray-to-EUV ratio observed in the Sun, assuming the same ratio for all spectral types and activity levels (thus age). The few observations of late type stars in the EUV contradict this view (e.g. Sanz-Forcada et al., 2003a). A better way to determine the radiation in the EUV range is to calculate a synthetic spectrum of each star using a coronal model. Such a model must describe accurately how the mass is distributed with temperature in the corona and transition region, the so-called Emission Measure Distribution (EMD). The EMD is complemented with the abundances of the different elements in the corona. If combined with an appropriate atomic model, it will be possible to predict the spectral energy distribution generated at coronal temperatures. Atomic models in this range have been tested only with solar data, and at the shorter wavelengths ( $\lambda \sim 100 - 400 \text{ \AA}$ ) with more active stars. We expect that a few lines formed at high temperature have inaccurate calculations or are missing from the models. But the bulk of the emission is already included in the models and the flux in a given range should be quite accurate. We use in our case the atomic model APED (Smith et al., 2001).

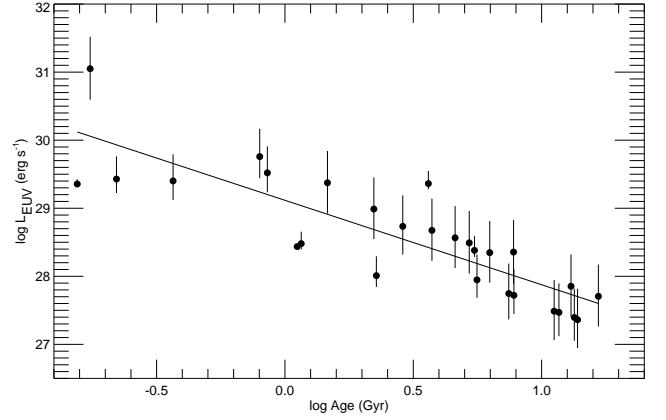


**Fig. 3.** Distribution of EUV luminosities against age (in Gyr) determined using the X-ray luminosities. The line indicates the best linear fit to the sample.

The atomic model needs to be folded with a coronal model. Fig. 1 shows the EMDs of three K2V stars with good high-resolution spectra, that allow us to construct an EMD with a resolution of 0.1 dex in temperature, following the method described in Sanz-Forcada et al. (2003b, and references therein). In general we do not have an accurate determination of the EMD for the stars in the sample, most of them limited to fits with less than 3 temperature components. Moreover, the observations in X-rays give us access only to the EM at  $T \geq 1 \text{ MK}$ , since lower temperature lines are rare in X-rays. However we cannot ignore the lower temperature part of the EMD, which corresponds to the transition region, because many lines in the EUV band are formed at  $T \leq 1 \text{ MK}$ . It is remarkable the case of the cooler He II 304  $\text{\AA}$  line, one of the strongest in the XUV spectrum of most cool stars.

#### 3.1. Transition region EMD

It is possible to calculate the EMD at  $T \leq 1 \text{ MK}$  by using lines in the UV (e.g. Dupree et al., 1993), but most of our objects have no UV spectra available. The large sample of EMDs reported by Sanz-Forcada et al. (2003a) showed that the “cool” side of the EMD is approximately proportional to the EMD at  $\log T (\text{K}) \sim 6 - 6.3$ . We checked that a reasonable proportionality exists among the values at these two temperature ranges (Appendix A). We have calibrated the relation using stars with known EMD at all temperatures, and extrapolated the lower temperature EMD, for the stars unobserved in UV, using this relation, as described in Appendix A. In particular we chose the EMD of the sample of stars in Sanz-Forcada et al. (2003a) that have well calculated EMD: we separated the sample in three groups depending on the level of activity (interpreted from the amount of EMD found at the highest temperatures). We define then three parameters: a parameter to account for the transformation between an EMD with 0.1 dex of temperature resolution and a 3T fit, the difference between the minimum of the EMD and the local maximum found at  $\log T (\text{K}) \sim 6.2 - 6.4$ , and the slope of the EMD at temperatures below the EMD minimum. We have then tested this extrapolation with one star of each of the three classes: AB Dor (Sanz-Forcada et al., 2003b),  $\epsilon$  Eri (Sanz-Forcada et al., 2004), and  $\alpha$  Cen B (Sect. B), all of them of type K2V (Fig. 1). The XUV flux calculated using a 3-T model ( $\log T (\text{K}) \geq 5.8$ ) and a synthetic EMD ( $\log T (\text{K}) < 5.8$ ), agrees in all cases within

**Table 5.** ROSAT X-ray (5–100 Å) and EUV (100–920 Å) luminosity of stars with exoplanets<sup>a</sup> (ROSAT). XUV includes the 5–920 Å range.

Planet name	Sp. type (star)	Stellar distance (pc)	$\log L_X$ (erg s <sup>-1</sup> )	$\log L_{EUV}$ (erg s <sup>-1</sup> )	$\log L_{bol}$ (erg s <sup>-1</sup> )	age (Gyr)	$M_p \sin i$ (m <sub>J</sub> )	$a_p$ (a.u.)	$\log F_X$ (erg s <sup>-1</sup> cm <sup>-2</sup> )	$\log F_{XUV}$ (erg s <sup>-1</sup> cm <sup>-2</sup> )	$\log F_X$ accum. (erg cm <sup>-2</sup> )	$\log F_{XUV}$ accum. (erg cm <sup>-2</sup> )	$\rho M_X$ (g <sup>2</sup> s <sup>-1</sup> cm <sup>-3</sup> ) <sup>b</sup>	$\rho M_{XUV}$ (g <sup>2</sup> s <sup>-1</sup> cm <sup>-3</sup> ) <sup>b</sup>
18 Del b	G6III	73.10 ± 3.74	29.33	30.02	35.11	...	10.30	2.60	1.05	1.82	...	...	1.3e+08	7.5e+08
1RXS1609 b	K7V	145 :	29.88	30.50	33.20	0.09	8.00	330.00	-2.61	-1.90	12.91	13.72	2.8e+04	1.4e+05
4 UMa b	K1III	77.40 ± 4.25	28.41	29.23	35.65	...	7.10	0.87	1.08	1.97	...	...	1.4e+08	1.0e+09
61 Vir b	G5V	8.53 ± 0.05	26.88	27.92	33.49	7.96	0.02	0.05	2.03	3.10	21.02	21.76	1.2e+09	1.4e+10
61 Vir c							0.06	0.22	0.76	1.83	19.75	21.76	6.4e+07	7.6e+08
61 Vir d							0.07	0.48	0.08	1.15	19.07	21.76	1.3e+07	1.6e+08
α Ari b	K2III	20.21 ± 0.40	27.19	28.18	35.51	...	1.80	1.20	-0.42	0.62	...	...	4.3e+06	4.7e+07
BD-10 3166 b	G4V	66 :	<29.20	<29.91	33.19	0.25	0.48	0.05	< 4.43	< 5.21	20.84	21.61	(3.0e+11)	(1.8e+12)
γ Cep b	K2IV	13.79 ± 0.10	<27.33	<28.30	34.63	4.08:	1.60	2.04	< -0.74	< 0.28	18.16:	18.62:	(2.0e+06)	(2.1e+07)
GJ 176 b	M2.5V	9.42 ± 0.22	27.41	28.37	31.74	3.62	0.03	0.07	2.32	3.33	20.12	21.43	2.4e+09	2.4e+10
GJ 832 b	M1.5V	4.94 ± 0.03	26.78	27.83	31.81	9.24	0.64	3.40	-1.73	-0.64	16.77	18.05	2.1e+05	2.5e+06
GJ 3021 b	G6V	17.62 ± 0.16	<28.95	<29.70	33.39	0.37	3.37	0.49	< 2.12	< 2.94	18.91	19.61	(1.5e+09)	(9.8e+09)
HD 3651 b	K0V	11.11 ± 0.09	27.27	28.25	33.36	4.46	0.20	0.28	0.91	1.94	19.47	20.23	9.2e+07	9.8e+08
HD 10647 b	F8V	17.35 ± 0.19	28.31	29.15	33.75	0.95	0.93	2.03	0.25	1.14	17.83	18.47	2.0e+07	1.6e+08
HD 38529 b	G4IV	42.43 ± 1.66	28.96	29.71	34.41	0.36:	0.78	0.13	3.28	4.09	20.42:	20.86:	2.1e+10	1.4e+11
HD 39091 b	G1IV	18.21 ± 0.15	27.49	28.44	33.74	3.22:	10.30	3.28	-0.99	0.01	17.44:	18.12:	1.1e+06	1.1e+07
HD 41004 A b	K1V	43.03 ± 1.89	<29.31	<30.01	33.36	0.22	2.54	1.64	< 1.43	< 2.21	17.79	18.50	(3.0e+08)	(1.8e+09)
HD 48265 b	G5V	87.41 ± 5.50	29.53	30.20	34.18	0.16	1.16	1.51	1.72	2.47	18.15	18.61	5.9e+08	3.3e+09
HD 70573 b	G1-1.5V	45.7 :	29.09	29.82	33.33	0.30	6.10	1.76	1.15	1.95	17.76	18.48	1.6e+08	1.0e+09
HD 87883 b	K0V	18.06 ± 0.31	27.60	28.54	33.10	2.73	12.10	3.60	-0.96	0.02	17.17	18.00	1.2e+06	1.2e+07
HD 89744 b	F7V	38.99 ± 1.06	28.11	28.97	34.38	1.28	7.20	0.88	0.77	1.69	18.79	19.28	6.6e+07	5.5e+08
HD 102365 b	G2V	9.24 ± 0.06	26.81	27.86	33.49	8.83	0.05	0.46	0.04	1.12	19.10	19.84	1.2e+07	1.5e+08
HD 128311 b	K0V	16.57 ± 0.27	28.48	29.29	33.06	0.74	2.18	1.10	0.95	1.82	18.13	18.95	1.0e+08	7.5e+08
HD 128311 c							3.21	1.76	0.54	1.41	17.72	18.95	3.9e+07	2.9e+08
HD 142415 b	G1V	34.57 ± 1.00	28.65	29.44	33.63	0.57	1.62	1.05	1.16	2.01	18.35	19.01	1.6e+08	1.2e+09
HD 147513 b	G3/G5V	12.87 ± 0.14	28.90	29.65	33.56	0.40	1.21	1.32	1.21	2.03	18.11	18.77	1.8e+08	1.2e+09
HD 150706 b	G0	27.23 ± 0.42	28.82	29.59	33.55	0.45	1.00	0.82	1.54	2.38	18.53	19.20	3.9e+08	2.7e+09
HD 169830 b	F8V	36.32 ± 1.20	28.26	29.10	34.23	1.02	2.88	0.81	0.99	1.90	18.80	19.32	1.1e+08	8.8e+08
HD 169830 c							4.04	3.60	-0.30	0.60	17.50	19.32	5.6e+06	4.5e+07
HD 176051 b	K1V	14.98 ± 0.12	<28.22	<29.07	32.86	1.09	1.50	1.76	< 0.28	< 1.19	17.67	18.56	(2.1e+07)	(1.7e+08)
HIP 75458 b	K2III	31.33 ± 0.50	27.41	28.37	35.38	...	8.82	1.27	-0.25	0.76	...	...	6.3e+06	6.4e+07
HIP 79431 b	M3V	14.90 ± 0.79	26.89	27.93	60.02	7.84	2.10	0.36	0.33	1.40	28.76	28.76	2.8e+07	2.8e+08
HR 810 b	G0V	17.24 ± 0.16	28.79	29.56	33.80	0.47	2.26	0.93	1.41	2.25	18.49	19.11	2.9e+08	2.0e+09

**Notes.** <sup>(a)</sup> Planet data from The Extrasolar Planets Encyclopedia (<http://exoplanet.eu>). <sup>(b)</sup> 1 M<sub>J</sub> Gyr<sup>-1</sup> = 6.02 × 10<sup>13</sup> g s<sup>-1</sup>

0.37 dex with that calculated using a complete EMD. Therefore we are confident that the method can be safely applied to the stars in our sample. As a comparison, the solar activity cycle spans 1.7 dex in X-ray luminosity (Orlando et al., 2001). We use also these stars to check how much flux we would be missing if we consider the EMD only above 1 MK, for the different levels of activity: we would miss a 3% of the flux (AB Dor, very active), 19% (intermediate activity ε Eri), and 40% (α Cen B, low activity). We conclude that the extension of the EMD to the cooler temperatures is necessary, especially for the less active stars. The reason is because in α Cen B 91% of the XUV flux is generated in the EUV band, while for AB Dor only 23% is in the EUV. Table 4 include the predicted flux in different bands of the EUV range, with a formal precision of 0.01 dex well below the expected cyclic variability of the stars.

The application of this calculation to the ROSAT data is not possible since we do not have a coronal model for these objects. Instead we calculated a direct relation between X-ray and EUV luminosities for all the XMM and Chandra objects in our sample that have an X-ray flux available (i.e., it is not an upper limit), with the EUV flux calculated as explained. A fit to these data (Fig. 2) yields:

$$\log L_{EUV} = (4.80 \pm 1.99) + (0.860 \pm 0.073) \log L_X \quad (3)$$

where  $L_X$  and  $L_{EUV}$  are the X-ray ( $\lambda\lambda$  5–100 Å) and EUV ( $\lambda\lambda$  100–920 Å) luminosities, in erg s<sup>-1</sup>. We have then applied this conversion to the ROSAT data. The calculated EUV luminosities are listed in Table 5.

### 3.2. EUV luminosity evolution with age

We have calibrated a relation of age- $L_{EUV}$  to calculate better the effects of the radiation in the whole XUV range. We have selected for the calibration all the stars in our sample, excluding those with only an upper limit of the X-ray flux, and stars that show a formal result with age larger than 20 Gyr (those with spectral type A and some M stars). The age determination is made with the X-ray luminosity as explained in next Section. The fit (Fig. 3) follows a power-law relation:

$$\log L_{EUV} = (29.12 \pm 0.11) - (1.24 \pm 0.15) \log \tau \quad (4)$$

where  $\tau$  is the age in Gyr. This relation has been used to calculate the accumulated effects of the coronal radiation in the planet atmosphere as listed in Tables 5, 6. Although Ribas et al. (2005) studied the time evolution of the EUV luminosity, this is the first time that a general relation age- $L_{EUV}$  has been calculated. Ribas et al. (2005) studied the spectral energy distributions of six solar analogs covering a wide range (0.1–6.7 Gyr) of stellar ages, in the X-rays and UV regimes. They used real spectra in the ranges 1–360 Å and 920–1950 Å as available. The distribution of stellar fluxes in the different bands with the stellar age was used to calibrate the time evolution of the high energy irradiance in these bands. The results were used to interpolate the evolution in the 360–920 Å band, resulting in a less steeper dependence (exponent  $\sim -1.0$  in this range,  $-1.20$  in 100–360 Å), than in our case ( $-1.24$  in 100–920 Å).

**Table 6.** X-ray (5–100 Å) and EUV (100–920 Å) luminosity of stars with exoplanets<sup>a</sup> (XMM-Newton and Chandra).

Planet name	Sp. type (star)	Stellar distance (pc)	$\log L_X$ (erg s <sup>-1</sup> )	$\log L_{\text{EUV}}$ (erg s <sup>-1</sup> )	$\log L_{\text{bol}}$ (erg s <sup>-1</sup> )	age (Gyr)	$M_p \sin i$ (m <sub>J</sub> )	$a_p$ (a.u.)	$\log F_X$ (erg s <sup>-1</sup> cm <sup>-2</sup> )	$\log F_{\text{XUV}}$ (erg s <sup>-1</sup> cm <sup>-2</sup> )	$\log F_X \text{accum.}$ (erg cm <sup>-2</sup> )	$\log F_{\text{XUV accum.}}$ (erg cm <sup>-2</sup> )	$\rho M_X$ (g s <sup>-1</sup> cm <sup>-3</sup> ) <sup>c</sup>	$\rho M_{\text{XUV}}$ (g s <sup>-1</sup> cm <sup>-3</sup> ) <sup>c</sup>
14 Her b	K0V	18.15 ± 0.19	26.92	27.75 <sup>+0.44</sup> <sub>-0.38</sub>	33.43	7.45	4.64	2.77	-1.41	-0.53	17.52	18.28	4.4e+05	3.3e+06
16 Cyg B b	G2.5V	21.62 ± 0.23	<26.71	<28.04	33.78	10.31	1.68	1.68	< -1.19	< 0.16	18.04	18.74	(7.2e+05)	(1.6e+07)
2M1207 b	M8	52.41 ± 1.10	<26.24	<27.16	30.07	< 15	4.00	46.00	< -4.53	< -3.56	13.71	15.78	(3.3e+02)	(3.1e+03)
30 Ari B b	F6V	39.43 ± 1.71	29.53	29.36 <sup>+0.07</sup> <sub>-0.03</sub>	33.83	0.16	9.88	1.00	2.09	2.31	18.35	18.93	1.4e+09	2.3e+09
47 UMa b	G0V	14.08 ± 0.13	25.45	26.56 <sup>+0.33</sup> <sub>-0.22</sub>	33.74	< 15	2.53	2.10	-2.64	-1.50	17.84	18.55	2.6e+04	3.6e+05
47 UMa c							0.54	3.60	-3.11	-1.97	17.37	18.08	8.8e+03	1.2e+05
47 UMa d							1.64	11.60	-4.12	-2.98	16.36	17.06	8.4e+02	1.2e+04
51 Peg b	G2IV	15.36 ± 0.18	<26.52	<27.86	33.65	13.50:	0.47	0.05	< 1.64	< 3.00	21.04:	21.76:	(4.9e+08)	(1.1e+10)
55 Cnc b	G8V	12.53 ± 0.13	26.65	27.49 <sup>+0.46</sup> <sub>-0.42</sub>	33.39	11.19	0.82	0.12	1.08	1.98	20.28	21.05	1.4e+08	1.1e+09
55 Cnc c							0.17	0.24	0.44	1.34	19.64	20.41	3.1e+07	2.4e+08
55 Cnc d							3.84	5.77	-2.32	-1.42	16.88	17.65	5.4e+04	4.2e+05
55 Cnc e							0.02	0.04	2.04	2.94	21.24	22.01	1.2e+09	9.7e+09
55 Cnc f							0.14	0.79	-0.59	0.31	18.61	19.38	2.9e+06	2.3e+07
β Pic b	A6V	19.28 ± 0.19	25.63	27.01 <sup>+0.44</sup> <sub>-0.39</sub>	34.49	...	8.00	12.00	-3.97	-2.58	...	...	1.2e+03	2.9e+04
ε Eridani b	K2V	3.22 ± 0.01	28.20	28.44 <sup>+0.00</sup> <sub>-0.00</sub>	33.10	1.12	1.55	3.39	-0.31	0.13	17.19	18.00	5.5e+06	1.5e+07
GJ 86 b	K1V	10.91 ± 0.07	<27.42	<29.15	33.16	3.59	4.01	0.11	< 1.88	< 3.63	20.23	21.04	(8.6e+08)	(4.8e+10)
GJ 317 b	M3.5	9.01 ± 0.97	26.12	27.43 <sup>+0.47</sup> <sub>-0.45</sub>	30.18	< 15	1.20	0.95	-1.28	0.05	17.15	19.15	5.9e+05	1.3e+07
GJ 436 b	M2.5	10.23 ± 0.24	25.96	26.87 <sup>+0.45</sup> <sub>-0.43</sub>	31.67	< 15	0.07	0.03	1.59	2.55	20.88	22.20	4.4e+08	4.0e+09
GJ 674 b	M2.5	4.54 ± 0.03	27.72	28.01 <sup>+0.38</sup> <sub>-0.38</sub>	31.54	2.27	0.04	0.04	3.09	3.56	20.42	21.86	1.4e+10	4.1e+10
GJ 876 b	M4V	4.70 ± 0.05	26.16	26.65 <sup>+0.41</sup> <sub>-0.31</sub>	31.37	< 15	2.28	0.21	0.07	0.69	19.04	20.48	1.3e+07	5.5e+07
GJ 876 c							0.71	0.13	0.48	1.10	19.45	20.89	3.4e+07	1.4e+08
GJ 876 d							0.02	0.02	2.07	2.69	21.04	22.48	1.3e+09	5.5e+09
GJ 876 e							0.05	0.33	-0.34	0.28	18.63	20.07	5.2e+06	2.1e+07
GQ Lup b	K7V	140 :	29.45	31.05 <sup>+0.47</sup> <sub>-0.45</sub>	33.36	0.17	21.50	103.00	-2.02	-0.41	14.16	14.87	1.1e+05	4.3e+06
HD 4308 b	G5V	21.85 ± 0.27	<25.94	<27.28	33.57	< 15	0.04	0.12	< 0.35	< 1.71	20.31	21.04	(2.5e+07)	(5.7e+08)
HD 20367 b	G0V	27.13 ± 0.79	29.29	29.43 <sup>+0.33</sup> <sub>-0.33</sub>	33.78	0.22	1.07	1.25	1.65	2.02	18.17	18.77	5.0e+08	1.2e+09
HD 27442 b	K2IV	18.23 ± 0.17	<26.14	<27.47	34.40	< 15	1.35	1.16	< -1.44	< -0.09	18.58:	19.12:	(4.1e+05)	(9.2e+06)
HD 46375 b	K1IV	33.41 ± 1.19	27.16	28.49 <sup>+0.47</sup> <sub>-0.45</sub>	33.48	5.22:	0.25	0.04	2.49	3.84	21.19:	21.93:	3.5e+09	7.7e+10
HD 49674 b	G5V	40.73 ± 1.89	27.41	29.36 <sup>+0.19</sup> <sub>-0.08</sub>	33.51	3.62	0.12	0.06	2.43	4.39	20.89	21.61	3.1e+09	2.8e+11
HD 50554 b	F8	31.03 ± 0.97	<26.32	<27.66	33.74	< 15	5.16	2.41	< -1.89	< -0.53	17.72	18.43	(1.4e+05)	(3.3e+06)
HD 52265 b	G0V	28.07 ± 0.66	26.89	27.72 <sup>+0.38</sup> <sub>-0.38</sub>	33.86	7.80	1.05	0.50	0.05	0.93	19.11	19.78	1.3e+07	9.7e+07
HD 70642 b	G5IV-V	28.76 ± 0.50	26.38	27.71 <sup>+0.47</sup> <sub>-0.44</sub>	33.58	< 15	2.00	3.30	-2.10	-0.76	17.41:	18.15:	8.9e+04	2.0e+06
HD 75289 b	G0V	28.94 ± 0.47	<25.90	<27.24	33.87	< 15	0.42	0.05	< 1.13	< 2.49	21.19	21.87	(1.5e+08)	(3.4e+09)
HD 93083 b	K3V	28.90 ± 0.84	26.90	28.36 <sup>+0.47</sup> <sub>-0.46</sub>	33.19	7.77	0.37	0.48	0.09	1.56	18.98	19.79	1.4e+07	4.1e+08
HD 95089 b	K0IV	139.08 ± 0.00	<27.09	<28.43	34.71	5.85:	1.20	1.51	< -0.72	< 0.64	18.46:	18.90:	(2.1e+06)	(4.9e+07)
HD 99492 b	K2V	17.99 ± 1.07	26.55	27.85 <sup>+0.47</sup> <sub>-0.45</sub>	33.11	13.01	0.11	0.12	0.92	2.24	20.14	20.98	9.3e+07	2.0e+09
HD 99492 c							0.36	5.40	-2.36	-1.04	16.85	17.70	4.9e+04	1.0e+06
HD 101930 b	K1V	30.50 ± 0.89	26.05	27.00 <sup>+0.39</sup> <sub>-0.28</sub>	33.27	< 15	0.30	0.30	-0.36	0.64	19.41	20.21	4.9e+06	4.9e+07
HD 102195 b	K0V	28.98 ± 0.97	28.43	29.76 <sup>+0.41</sup> <sub>-0.41</sub>	33.26	0.80	0.45	0.05	3.60	4.95	20.91	21.67	4.5e+10	1.0e+12
HD 108147 b	F8/G0V	38.57 ± 1.03	27.39	28.67 <sup>+0.37</sup> <sub>-0.45</sub>	33.85	3.74	0.26	0.10	1.92	3.23	20.48	21.14	9.4e+08	1.9e+10
HD 111232 b	G8V	28.88 ± 0.67	<26.35	<27.69	33.40	< 15	6.80	1.97	< -1.69	< -0.33	17.81	18.59	(2.3e+05)	(5.3e+06)
HD 114386 b	K3V	28.04 ± 1.04	26.53	27.40 <sup>+0.42</sup> <sub>-0.41</sub>	33.02	13.41	1.24	1.65	-1.36	-0.43	17.85	18.72	5.0e+05	4.1e+06
HD 114762 b	F9V	40.57 ± 2.37	<26.51	<27.83	33.76	13.73	11.68	0.36	< -0.06	< 1.28	19.37	20.07	(9.9e+06)	(2.1e+08)
HD 114783 b	K0V	20.43 ± 0.44	<26.54	<27.83	33.19	13.17	1.00	1.20	< -1.07	< 0.24	18.18	19.01	(9.6e+05)	(2.0e+07)
HD 130322 b	K0V	29.76 ± 1.34	27.25	28.57 <sup>+0.47</sup> <sub>-0.47</sub>	33.28	4.60	1.02	0.09	1.91	3.25	20.47	21.25	9.2e+08	2.0e+10
HD 154345 b	G8V	18.06 ± 0.18	27.12	27.95 <sup>+0.37</sup> <sub>-0.26</sub>	33.36	5.60	0.95	4.19	-1.58	-0.69	17.14	17.90	3.0e+05	2.3e+06
HD 164922 b	K0V	21.93 ± 0.34	<25.74	<27.08	33.44	< 15	0.36	2.11	< -2.35	< -1.00	17.77	18.53	(5.0e+04)	(1.1e+06)
HD 179949 b	F8V	27.05 ± 0.59	28.38	29.52 <sup>+0.39</sup> <sub>-0.29</sub>	33.84	0.85	0.95	0.05	3.63	4.80	21.15	21.78	4.8e+10	7.0e+11
HD 187123 b	G5	47.92 ± 1.63	<27.24	<28.62	33.78	4.67	0.52	0.04	< 2.53	< 3.93	21.22	21.90	(3.8e+09)	(9.6e+10)
HD 187123 c							1.99	4.89	< -1.59	< -0.19	17.11	17.78	(2.9e+05)	(7.3e+06)
HD 189733 b	K1-K2	19.25 ± 0.32	28.18	28.48 <sup>+0.18</sup> <sub>-0.08</sub>	33.10	1.16	1.15	0.03	3.73	4.21	21.26	22.07	6.1e+10	1.8e+11
HD 190360 b	G6IV	15.89 ± 0.16	<26.35	<27.69	33.65	< 15	1.50	3.92	< -2.29	< -0.93	17.28:	18.00:	(5.8e+04)	(1.3e+06)
HD 190360 c							0.06	0.13	< 0.69	< 2.05	20.25:	20.98:	(5.5e+07)	(1.3e+09)
HD 195019 b	G3IV-V	37.36 ± 1.24	<26.23	<27.57	33.89	< 15	3.70	0.14	< 0.50	< 1.86	20.24:	20.92:	(3.5e+07)	(8.1e+08)
HD 209458 b	G0V	47.08 ± 2.22	<26.40	<27.74	33.78	< 15	0.71	0.05	< 1.60	< 2.96	21.14	21.84	(4.5e+08)	(1.0e+10)
HD 216435 b	G0V	33.29 ± 0.81	27.74	28.99 <sup>+0.47</sup> <sub>-0.44</sub>	34.14	2.22	1.26	2.56	-0.53	0.75	17.78	18.35	3.3e+06	6.3e+07
HD 216437 b	G4IV-V	26.52 ± 0.41	26.62	27.47 <sup>+0.42</sup> <sub>-0.35</sub>	33.92	11.68:	1.82	2.32	-1.56	-0.65	17.80:	18.47:	3.1e+05	2.5e+06
HD 217107 b	G8IV	19.72 ± 0.29	<25.50	<26.84	33.64	< 15	1.33	0.07	< 0.32	< 1.68	20.74:	21.46:	(2.4e+07)	(5.4e+08)
HD 217107 c							2.49	5.27	< -3.40	< -2.03	17.02:	17.75:	(4.5e+03)	(1.0e+05)
HD 218566 b	K3V	29.94 ± 1.07	27.04	28.35 <sup>+0.47</sup> <sub>-0.44</sub>	33.13	6.28	0.21	0.69	-0.08	1.25	18.64	19.47	9.3e+06	2.0e+08
HD 330075 b	G5	50.20 ± 3.75	26.51	27.36 <sup>+0.46</sup> <sub>-0.42</sub>	33.26	13.80	0.62	0.04	1.88	2.79	21.18	21.99	8.5e+08	6.9e+09
HR 8799 b	A5V	39.94 ± 1.36	28.02	29.37 <sup>+0.47</sup> <sub>-0.45</sub>	34.26	...	7.00	68.00	-3.09	-1.72	...	...	9.0e+03	2.1e+05
HR 8799 c							10.00	38.00	-2.59	-1.22	...	...	2.9e+04	6.8e+05
HR 8799 d							10.00	24.00	-2.19	-0.82	...	...	7.3e+04	1.7e+06
HR 8799 e							9.00	14.50	-1.75	-0.38	...	...	2.0e+05	4.7e+06
μ Ara b	G3IV-V	15.28 ± 0.19	<25.99	<27.32	33.83	< 15	1.68	1.50	< -1.81	< -0.46	18.15:	18.84:	(1.7e+05)	(3.9e+06)
μ Ara c							0.03	0.09	< 0.62	< 1.97	20.59:	21.28:	(4.7e+07)	(1.1e+09)
μ Ara d							0.52	0.92	< -1.39	< -0.04	18.58:	19.27:	(4.6e+05)	(1.0e+07)
μ Ara e							1.81	5.24	< -2.90	< -1.55	17.07:	17.76:	(1.4e+04)	(3.2e+05)
NGC 2423 3 b		766 :	<29.27	<34.91	35.54	0.23	10.60	2.10	< 1.18	< 6.82	18.45	18.64	(1.7e+08)	(7.4e+13)
Pollux b	K0III	10.34 ± 0.09	27.13	28.38 <sup>+0.21</sup> <sub>-0.19</sub>	35.19	...	2.90	1.69	-0.77	0.50	...	...	1.9e+06	3.6e+07
τ Boo b	F7V	15.60 ± 0.17	28.95	29.40 <sup>+0.39</sup> <sub>-0.28</sub>	34.06	0.37	3.90	0.05	4.18	4.76	21.19	21.72	1.7e+11	6.4e+11
ν And b	F8V	13.47 ± 0.13	27.56	28.73 <sup>+0.46</sup> <sub>-0.41</sub>	34.11	2.88	0.69	0.06	2.57	3.77	21.04	21.63	4.2e+09	6.6e+10
ν And c							14.57	0.86	0.25	1.44	18.72	19.30	2.0e+07	3.1e+08
ν And d							1							

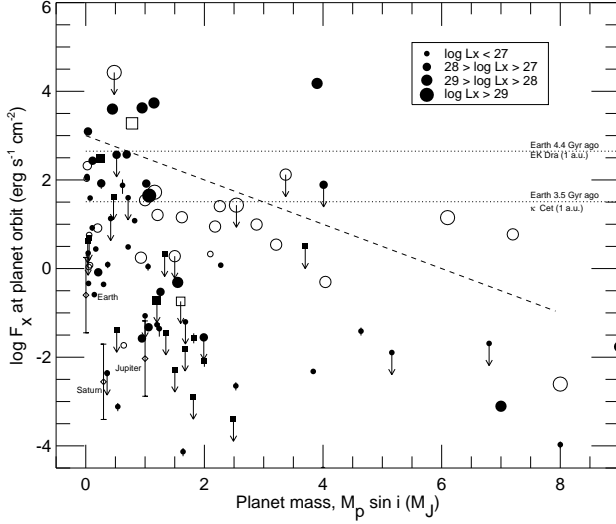


**Fig. 4.** Distribution of planetary masses ( $M_p \sin i$ ) with X-ray flux at the planet orbit. Filled symbols (squares for subgiants, circles for dwarfs) are XMM-Newton and Chandra data. Arrows indicate upper limits. Open symbols are ROSAT data without error bars. Diamonds represent Jupiter, Saturn, and the Earth. The dashed line marks the “erosion line” that might separate the phases of strong and weak evaporation (Paper I). Dotted lines indicate the X-ray flux of the younger Sun at 1 a.u.

#### 4. Results

Processes of mass loss in the atmosphere of a planet are not well understood. Once the circumstellar disc is dissipated it is expected that thermal losses are dominant. The mass loss rate due to thermal losses in a planet with an atmosphere mostly composed by hydrogen is defined by Eq. 2. To account for all the energy budget in the XUV band we need to know the radiation that is absorbed by neutral hydrogen, i.e., photons with  $\lambda < 912 \text{ \AA}$ . In Paper I we considered only the X-rays photons as a proxy of the whole XUV radiation. It is thus necessary to test whether the conclusions achieved hold also for the whole XUV range. With all the energy budget we can make a first estimate of the total mass lost due to thermal losses for the planets in the sample with known density (see below). Figures 4 and 5 show the distribution of planet masses ( $M_p \sin i$ ) with the X-ray flux at the planet orbit (directly measured) and the XUV flux that we have calculated after modeling of corona and transition region. A dashed line ( $\log F_X = 3 - 0.5 M_p \sin i$ ) is plotted in Figure 4 to indicate the “erosion line”, proposed in Paper I to separate what could be a regime of fast erosion from a slower erosion phase, based on the observed distribution. Fig. 5 is a direct indication of the current mass loss rate in exoplanets, assuming that thermal losses are dominant and the density is the same for all planets (according to Eq. 2). Regrettably we know the planet density of only four planets in our sample (Table 7). Rocky planets ( $\rho \sim 5 \text{ g cm}^{-3}$ ) are not supposed to be affected in the same manner (a gaseous planet like Jupiter has  $\rho=1.24$ ). We marked in the plot the XUV flux that would have arrived at the Earth’s orbit at an age of  $\sim 100 \text{ Myr}$  and  $\sim 1 \text{ Gyr}$ . To calculate this flux we used two young solar analogs,  $\kappa \text{ Cet}$  and  $\text{EK Dra}$ , as explained in Paper I. The emission in the EUV range was calculated by Sanz-Forcada et al. (in prep.) extrapolating from a coronal model determined with high resolution spectra.

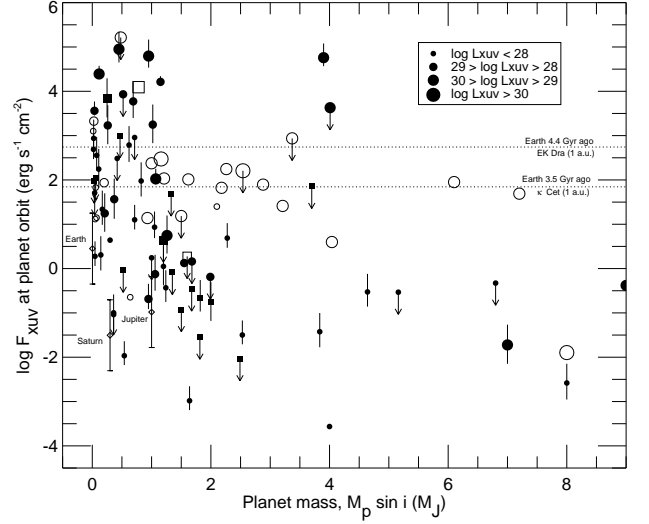


**Fig. 5.** Distribution of planetary masses ( $M_p \sin i$ ) with XUV flux at the planet orbit. Symbols as in Fig. 4. Error bars indicate the limits in EUV flux calculated with the models. Dotted lines indicate the X-ray flux of the younger Sun at 1 a.u. Note that mass loss rates increase with the XUV flux.

A better way to measure the long-term effects of the radiation is to calculate the accumulated XUV flux at the orbit of the planet. To do that we need to know how coronal radiation evolves with time. Several laws have been reported in the past, mostly devoted to explain the coronal history of the Sun as a law of the kind  $L_X \sim t^\alpha$ , calibrated with G dwarfs. Some examples are Maggio et al. (1987,  $\alpha = -1.5$ ), Ayres (1997,  $\alpha = -1.74$ ), Guedel et al. (1997,  $\alpha = -1.5$ ), Ribas et al. (2005,  $\alpha = -1.27$  or  $-1.92$ , for  $1\text{--}20 \text{ \AA}$  and  $20\text{--}100 \text{ \AA}$  respectively), Penz et al. (2008,  $\alpha = -1.69$ ), and Penz & Micela (2008,  $\alpha = -1.34$ , calibrated with M dwarfs). We use the law by Garcés et al. (in prep.), calibrated with late F to early M dwarfs:

$$\begin{aligned} L_X &= 6.3 \times 10^{-4} L_{\text{bol}} & (\tau < \tau_i) \\ L_X &= 1.89 \times 10^{28} \tau^{-1.55} & (\tau > \tau_i) \end{aligned} \quad (5)$$

with  $\tau_i = 2.03 \times 10^{20} L_{\text{bol}}^{-0.65}$ .  $L_X$  and  $L_{\text{bol}}$  are in  $\text{erg s}^{-1}$ , and  $\tau$  is the age in Gyr. The  $\tau_i$  parameter marks the typical change from saturation regime to an inverse proportionality between  $L_X/L_{\text{bol}}$  and rotation period (e.g. Pizzolato et al., 2003). The relation shows a similar behavior to former calibrations, but it can be applied to a wider range of stellar masses. We use Eq. 5 to calculate the stellar age (Table 6), with the caveat that there is an uncertainty of about an order of magnitude in the  $L_X$  levels of stars of the same spectral type and age (Penz et al., 2008; Penz & Micela, 2008), and that the solar cycle in X-rays spans as much as 1.7 dex in  $L_X$  (Orlando et al., 2001). We consider a formal upper limit of the age at 15 Gyr (current estimate of the age of the Universe is 13.7 Gyr, Bennett et al., 2003). This method is not optimal for the age determination of a star, but it is more appropriate if we want to know the “X-ray age” in the evolution of the coronal emission of a given star.

The accumulated X-ray and XUV flux at the planet orbit (Table 6, Fig. 6) is calculated using Eqs. 4 and 5, between 20 Myr and the present. Most protoplanetary discs would have dissipated after 20 Myr. We do not calculate the age for giants and A-type stars, and mark the subgiants with different symbols since it is not known whether they follow the same relation, but sometimes the determination of the star as dwarf or subgiant is not precise.

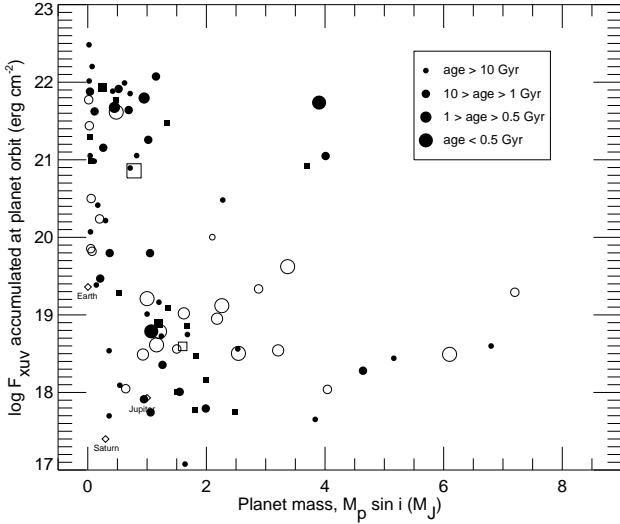


**Fig. 6.** Distribution of planetary masses ( $M_p \sin i$ ) with the XUV flux accumulated at the planet orbit since an age of 20 Myrs to the present day (see text). Symbols as in Fig. 4. Note that increasing XUV flux accumulated indicates a larger mass lost to date.

Only planets with  $M \sin i < 9 M_J$  are considered for further calculations. According to Eq. 2, Fig. 6 is a direct indication of the total mass lost to date, assuming same density for all planets. A planet like  $\tau$  Boo b, with  $10^{21.7} \text{ erg cm}^{-2}$  accumulated in the XUV band during 350 Myr, would have lost  $\sim 0.04 M_J$  if the density is  $1 \text{ g cm}^{-3}$ , but as much as  $\sim 0.7 M_J$  if the density is  $0.1 \text{ g cm}^{-3}$ , among the lowest observed in exoplanets.

#### 4.1. Accumulated effects in planets with known density

It is expected that the accumulated effects of the XUV radiation result in a population of close-in planets with less massive planets, unless they have higher densities, or they simply have little or no atmosphere. The current distribution of planets with known density is dominated by close-in planets, and therefore it has an appropriate bias to test these effects, even if we do not know the radiation of their parent stars. It is remarkable to observe in such distribution that there are no massive planets with low density at short distances of the star (Paper I). We do not know now if this is also applicable for planets at further distances, that would indicate that this is an effect of planet formation. Theoretical models (e.g. Guillot, 2005; Fortney et al., 2007) indicate that irradiated planets might have a nearly constant radius for planets with  $M_p \gtrsim 1 M_J$ , explaining the increasing density with mass in Fig. 3 of Paper I. The radius-mass relation of the same sample supports this idea (Fig. 7), although actual values of planet radius are slightly higher on average than Fig. 10 of Guillot (2005). This empirical relation can be defined as follows:

$$\begin{aligned} R_p &= (0.15 \pm 0.07) + (4.1 \pm 3.0)M_p & (M_p < 0.05) \\ R_p &= (0.29 \pm 0.11) + (2.45 \pm 0.36)M_p & (0.05 < M_p < 0.5) \\ R_p &= (1.23 \pm 0.05) + (0.00 \pm 0.02)M_p & (0.5 < M_p < 4.5) \end{aligned} \quad (6)$$

With the estimate of the total XUV flux it is possible now to check the mass loss history of the few planets in our sample with known density (we exclude the A5V star HR 8799).

While 2M1207 b suffers basically no erosion (Table 6), the other three planets (GJ 436 b, HD 189733 b, HD 209458 b) show that strong mass loss takes place. Since we know the stellar and planet parameters for these cases we can also calculate the mass loss through the Roche Lobe point. The formula in Eq. 1 would be then

$$\dot{M}_{\text{XUV}} \sim \frac{3F_{\text{XUV}}}{4GK\rho}. \quad (7)$$

where the  $K$  parameter is defined as a function of  $R_p$ ,  $M_p$  (planet radius and mass),  $a_p$  (semimajor axis) and  $M_*$  (stellar mass), as described in Erkaev et al. (2007). Table 7 list the parameters used in the calculation. Note that Erkaev et al. (2007) calculates the wrong values of  $K$ , likely because of a mistake in the substitution of the units used to determine the Roche lobe distance, overestimating the mass losses through the Roche lobe. Fig. 8 represents the mass loss history, assuming that planet density remains constant and only thermal losses are eroding the atmosphere. We consider also the hypothesis of mass losses following the same trend (constant radius for HD 209458 b, HD 189733 b and 2M1207 A b,  $R_p \sim 2.45 M_p$  for GJ 436) found in the mass-radius relation of close-in planets (Eq. 6), in better agreement with theoretical models. Future development of Eq. 7 should give a more accurate view of the thermal losses. In this sense Lammer et al. (in prep., see also Lammer et al., 2009) multiply Eq. 7 by the heating efficiency (about 10–25%). This would imply much lower effects of evaporation, but it is insufficient to justify the mass loss rate measured in HD 209458 b (see below). Other models include different effects of EUV radiation in the atmosphere, and infrared cooling (Yelle, 2004; Tian et al., 2005; García Muñoz, 2007; Murray-Clay et al., 2009), usually yielding smaller escape rates than Eq. 7. Those models are not easy to test with our sample, and they do not consider the effects of X-rays.

## 5. Discussion

The distribution of planets with the X-ray flux received seems to indicate that planets have lost mass in their first stages. Fig. 4 can be interpreted in the same manner as an HR diagram: the lack of planets in a given area of the diagram indicates that they spend little time in that phase, while the accumulation of planets in other area indicates that they spend much time in that position. We can divide the diagram in four boxes based on the mass (at  $1.5 M_J$ ) and the X-ray flux at the planet orbit (at  $\log F_X = 2.15$ ). We see then that only 1 out of 12 of the planets with high flux have a high mass, while 38 out of 84 (45%) of the planets receiving lower fluxes have a high mass (up to  $9 M_J$  in this diagram). Therefore it is clear the absence of high mass planets suffering high flux levels. The same exercise is applicable to Fig. 5.

To explain this distribution we propose three alternatives: (i) an observational bias, (ii) an effect of planet formation, and (iii) a physical phenomenon that moves the planets from their original positions in the diagram. The observational biases (discussed in Paper I) easily explain the lack of planets in the lower left corner of the diagram, corresponding to low mass planets at long distances from the star. But the same biases should make us find more planets in the upper right corner, where no planets are found. The second possibility, the effects of planet formation, can not be easily identified at the present level of knowledge. Simulations carried out by, e.g., Mordasini et al. (2009) do not cover planets with  $a_p < 0.1 \text{ a.u.}$  and more recent simulations (Benítez-Llambay et al., 2011) might justify only the gap observed in the mass-distance diagram at  $M \lesssim 1 M_J$  and



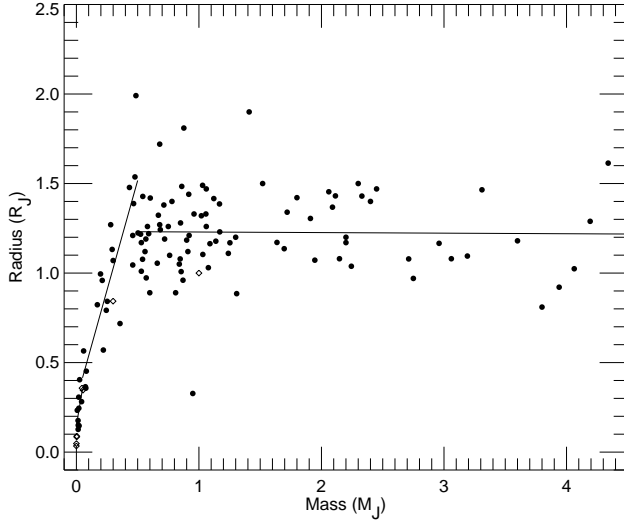


**Fig. 7.** Mass-radius relation in the sample of exoplanets (8 Mar 2011) of known radius (filled circles). Open diamonds represent the Solar System planets. Solid lines indicate the least-square fit to the data (see text).

**Table 7.** Mass lost in planets with known density

Planet name	$R_p$ ( $R_J$ )	$M_p$ ( $M_J$ )	$\rho$ ( $\text{g cm}^{-3}$ )	$M_*$ ( $M_\odot$ )	$a_p$ (a.u.)	$K^a$	$M_{\text{lost}}^b$ (1)	$M_{\text{lost}}^b$ (2)
GJ 436 b	0.365	0.0737	1.88	0.452	0.0289	0.76	0.06	0.08
HD 189733 b	1.151	1.15	0.94	0.8	0.0314	0.67	0.11	0.11
HD 209458 b	1.38	0.714	0.34	1.0	0.0475	0.65	0.18	0.17
2M1207 A b	1.5	4.0	1.47	0.025	46	1.00	2e-8	2e-8

**Notes.** <sup>(a)</sup>  $K$  parameter to account for the Roche Lobe effects as in Eq. 7. <sup>(b)</sup> Mass lost since 20 Myr old, including Roche lobe effects and thermal losses. (1) is for constant density, (2) with  $M - R$  relation as explained in the text

$a_p \lesssim 0.04$  a.u. The effects of X-rays in an eventual photo-evaporation of the protoplanetary disc has been analyzed by Drake et al. (2009) and Owen et al. (2011). If planet formation favors presence of low mass planets close to the star, Figs. 4 and 5 just reflect a lack of high mass population at short distances ( $F_X \propto d^{-2}$ ). However the distribution of density with mass at short distance of the star (Paper I) reveals that such population exists (32% of the 120 planets currently in the sample have  $M > 1.5 M_J$ ), but they have an increasing density with mass, an important detail also for (iii). Finally there exists the possibility that one or several physical processes related to the XUV emission (and X-rays as a proxy) are eroding the atmospheres of planets at close distances to the star, yielding in the long term an uneven distribution of masses with  $F_X$ . The Eq. 2 indicates also that planet density provides protection against thermal losses, consistent with the observed trend in the mass-density diagram just mentioned. The distribution of masses with the XUV flux accumulated over time (Fig. 6) further supports the interpretation of mass losses as the effect of XUV irradiation, either by thermal or non-thermal effects: most massive exoplanets that were initially exposed to high radiation would have now less than  $1.5 M_J$ .

The upper limit of the hydrogen mass loss rate we calculate for HD 209458 b ( $1 \times 10^{10} \text{ g s}^{-1}$ ) is consistent with the values of  $\sim 10^{10} \text{ g s}^{-1}$  (Vidal-Madjar et al., 2003) interpreted by

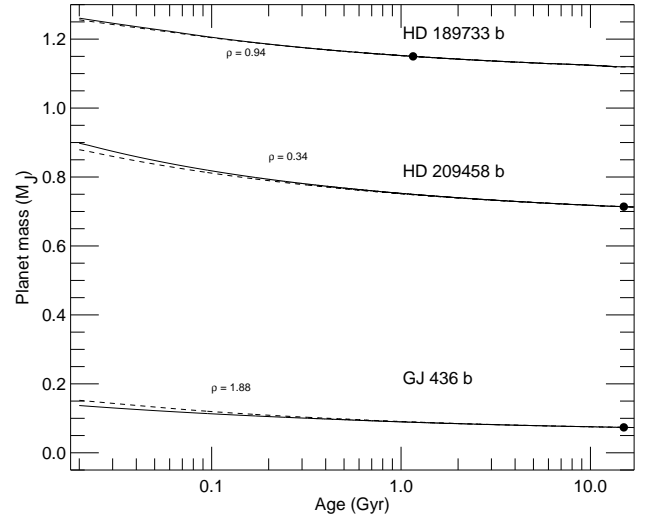


**Fig. 8.** Time evolution of planetary mass, assuming thermal and Roche lobe losses. Planet density is indicated. Solid lines indicate evolution under constant density conditions, while dashed lines consider the radius-mass relation as explained in the text (constant radius if  $M_p > 0.5 M_J$ ). Current age is marked with solid circles.

the authors as hydrogen escaping the planet atmosphere, and with the calculation of  $\sim 8 \times 10^{10} \text{ g s}^{-1}$  extrapolated from C II line absorption by Linsky et al. (2010). Similarly our calculation for HD 189733 ( $2 \times 10^{11} \text{ g s}^{-1}$ ) is consistent with the value of  $\sim 10^{11} \text{ g s}^{-1}$  estimated by Lecavelier Des Etangs et al. (2010). Further support for our interpretation is found if we look at the chromosphere: Hartman (2010) finds that there is a correlation between chromospheric activity and planet surface gravity. Contrary to the statement by Scharf (2010), this relation supports our conclusions, since denser planets also have a stronger surface gravity. Therefore the accumulated effects of erosion over time favor a resulting distribution with denser (and with higher surface gravity) planets close to active stars.

The presence of an “erosion line” (Fig. 4) that might separate the stages of strong and weak evaporation (Paper I), cannot be precisely quantified until we have a large sample of planets with known density and X-ray measurements of their parent stars. It is possible that such a line separates the phase of heavy erosion of a planet from that of slow or no erosion. The establishment of such a line would be interesting for future works to test whether a planet is still suffering strong erosion. Planets above the line are potential targets to detect atmospheric features.

## 6. Conclusions

The bulk of evidence support the effects of erosion on planet atmospheres, as an effect of XUV radiation. The accumulated effects of evaporation by radiation yield a population of only low mass planets exposed to a currently high XUV radiation. This interpretation is also supported by the lack of low density massive planets among the close-in planets population. We have used a simple physical model to test the observed distribution. This model assumes that mass losses are controlled by the thermal evaporation due to the XUV radiation absorbed in the atmosphere. In the four planets of the sample with known density we have reconstructed the mass loss history, starting at a stellar age of 20 Myr, including thermal losses and losses through the

Roche lobe. The density protects the planet atmosphere from further losses, but in a low density planet such as HD 209458b, up to  $\sim 0.2 M_J$  have been lost according to this model. Future model developments should take into account non-thermal losses, the role of planetary magnetic field, and impact of different atmospheric composition. This research will benefit from the future inclusion of a larger population of planets with known density and X-ray stellar emission.

**Acknowledgements.** JSF and DGA acknowledge support from the Spanish MICINN through grant AYA2008-02038 and the Ramón y Cajal Program ref. RYC-2005-000549. IR acknowledges support from the Spanish MICINN via grant AYA2006-15623-C02-01. GM acknowledges financial contribution from PRIN/INAF (P.I.: Lanza). This research has made use of the NASA's High Energy Astrophysics Science Archive Research Center (HEASARC) and the public archives of XMM-Newton and Chandra. We are grateful to the anonymous referee and to the editor, T. Guillot, for the careful reading of and useful comments on the manuscript.

## References

- Anders, E. & Grevesse, N. 1989, *Geochim. Cosmochim. Acta*, 53, 197
- Asplund, M., Grevesse, N., & Sauval, A. J. 2005, in *ASP Conf. Series*, Vol. 336, *Cosmic Abundances as Records of Stellar Evolution and Nucleosynthesis*, ed. T. G. Barnes, III & F. N. Bash, 25
- Ayres, T. R. 1997, *J. Geophys. Res.*, 102, 1641
- Baraffe, I., Selsis, F., Chabrier, G., et al. 2004, *A&A*, 419, L13
- Benítez-Llambay, P., Masset, F., & Beaugé, C. 2011, *A&A*, 528, A2
- Bennett, C. L., Halpern, M., Hinshaw, G., et al. 2003, *ApJS*, 148, 1
- Cecchi-Pestellini, C., Ciaravella, A., Micela, G., & Penz, T. 2009, *A&A*, 496, 863
- Cox, A. N. 2000, *Allen's astrophysical quantities*, ed. Cox, A. N.
- Drake, J. J., Ercolano, B., Flaccomio, E., & Micela, G. 2009, *ApJ*, 699, L35
- Dupree, A. K., Brickhouse, N. S., Doschek, G. A., Green, J. C., & Raymond, J. C. 1993, *ApJ*, 418, L41
- Erkaev, N. V., Kulikov, Y. N., Lammer, H., et al. 2007, *A&A*, 472, 329
- Flower, P. J. 1996, *ApJ*, 469, 355
- Fortney, J. J., Marley, M. S., & Barnes, J. W. 2007, *ApJ*, 659, 1661
- García Muñoz, A. 2007, *Planet. Space Sci.*, 55, 1426
- Guedel, M., Guinan, E. F., & Skinner, S. L. 1997, *ApJ*, 483, 947
- Guillot, T. 2005, *Annual Review of Earth and Planetary Sciences*, 33, 493
- Hartman, J. D. 2010, *ApJ*, 717, L138
- Houck, J. C. & Denicola, L. A. 2000, in *Astronomical Society of the Pacific Conference Series*, Vol. 216, *Astronomical Data Analysis Software and Systems IX*, ed. N. Manset, C. Veillet, & D. Crabtree, 591
- Huenemoerder, D. P., Canizares, C. R., Drake, J. J., & Sanz-Forcada, J. 2003, *ApJ*, 595, 1131
- Huensch, M., Schmitt, J. H. M. M., & Voges, W. 1998, *A&AS*, 132, 155
- Jaritz, G. F., Endler, S., Langmayr, D., et al. 2005, *A&A*, 439, 771
- Kashyap, V. L., Drake, J. J., & Saar, S. H. 2008, *ApJ*, 687, 1339
- Lammer, H., Odert, P., Leitzinger, M., et al. 2009, *A&A*, 506, 399
- Lammer, H., Selsis, F., Ribas, I., et al. 2003, *ApJ*, 598, L121
- Lecavelier Des Etangs, A. 2007, *A&A*, 461, 1185
- Lecavelier Des Etangs, A., Ehrenreich, D., Vidal-Madjar, A., et al. 2010, *A&A*, 514, A72
- Lecavelier des Etangs, A., Vidal-Madjar, A., McConnell, J. C., & Hébrard, G. 2004, *A&A*, 418, L1
- Linsky, J. L., Yang, H., France, K., et al. 2010, *ApJ*, 717, 1291
- Maggio, A., Sanz-Forcada, J., & Scelsi, L. 2011, *A&A*, 527, A144
- Maggio, A., Sciortino, S., Vaiana, G. S., et al. 1987, *ApJ*, 315, 687
- Mordasini, C., Alibert, Y., & Benz, W. 2009, *A&A*, 501, 1139
- Murray-Clay, R. A., Chiang, E. I., & Murray, N. 2009, *ApJ*, 693, 23
- Orlando, S., Peres, G., & Reale, F. 2001, *ApJ*, 560, 499
- Owen, J. E., Ercolano, B., & Clarke, C. J. 2011, *MNRAS*, 412, 13
- Penz, T. & Micela, G. 2008, *A&A*, 479, 579
- Penz, T., Micela, G., & Lammer, H. 2008, *A&A*, 477, 309
- Pizzolato, N., Maggio, A., Micela, G., Sciortino, S., & Ventura, P. 2003, *A&A*, 397, 147
- Poppenhaeger, K., Robrade, J., & Schmitt, J. H. M. M. 2010, *A&A*, 515, A98
- Raassen, A. J. J., Ness, J., Mewe, R., et al. 2003, *A&A*, 400, 671
- Ribas, I., Guinan, E. F., Güdel, M., & Audard, M. 2005, *ApJ*, 622, 680
- Sanz-Forcada, J., Brickhouse, N. S., & Dupree, A. K. 2002, *ApJ*, 570, 799
- Sanz-Forcada, J., Brickhouse, N. S., & Dupree, A. K. 2003a, *ApJS*, 145, 147
- Sanz-Forcada, J., Favata, F., & Micela, G. 2004, *A&A*, 416, 281
- Sanz-Forcada, J., García-Álvarez, D., Velasco, A., et al. 2010a, in *IAU Symposium*, Vol. 264, *IAU Symposium*, ed. A. G. Kosovichev, A. H. Andrei, & J.-P. Roelot, 478–483
- Sanz-Forcada, J., Maggio, A., & Micela, G. 2003b, *A&A*, 408, 1087
- Sanz-Forcada, J. & Micela, G. 2002, *A&A*, 394, 653
- Sanz-Forcada, J., Ribas, I., Micela, G., et al. 2010b, *A&A*, 511, L8
- Scharf, C. A. 2010, *ApJ*, 722, 1547
- Schmitt, J. H. M. M., Fleming, T. A., & Giampapa, M. S. 1995, *ApJ*, 450, 392
- Smith, R. K., Brickhouse, N. S., Liedahl, D. A., & Raymond, J. C. 2001, *ApJ*, 556, L91
- Tian, F., Toon, O. B., Pavlov, A. A., & De Sterck, H. 2005, *ApJ*, 621, 1049
- Vidal-Madjar, A., Lecavelier des Etangs, A., Désert, J.-M., et al. 2003, *Nature*, 422, 143
- Watson, A. J., Donahue, T. M., & Walker, J. C. G. 1981, *Icarus*, 48, 150
- Winn, J. N., Holman, M. J., Henry, G. W., et al. 2007, *AJ*, 133, 1828
- Yelle, R. V. 2004, *Icarus*, 170, 167

## Appendix A: Extrapolation of the lower temperature EMD

The determination of the EMD in the transition region ( $\log T$  [K]  $\sim 4.2 - 5.8$ ) usually benefits from the information provided by UV lines. For the sources with no UV spectroscopic observations we need to develop a method to calculate the EMD in this region. We extrapolate the values of the EMD at those temperatures based on the coronal counterpart, for which a general proportionality seems to be present. Both transition region and coronal material are supposed to be part of the same geometrical structures (loops). In the coronal EMD of all sources we can identify the presence of material at  $\log T$  [K]  $\sim 6.3$ , the typical temperature of the solar corona, despite of their activity level. We use the EM level at that peak, averaged over three values of  $T$ , to calibrate the relation to the lower temperature EMD. We used a sample of objects with a well calculated EMD over the whole range, using same technique in all cases (Sanz-Forcada et al., 2002; Sanz-Forcada & Micela, 2002; Sanz-Forcada et al., 2003a; Huenemoerder et al., 2003; Sanz-Forcada et al., 2004), and adding  $\alpha$  Cen B (Sect. B). We separated the sample in three groups depending on the level of activity (interpreted from the amount of EMD found at the highest temperatures): low activity stars (group 1: Procyon,  $\alpha$  Cen B), moderately active stars (group 2:  $\epsilon$  Eri,  $\xi$  UMa B), and active stars (group 3: VY Ari,  $\sigma^2$  CrB, AR Lac, FK Aqr, AD Leo, UX Ari, V711 Tau, II Peg, AB Dor).

The lower temperature EMD can be defined using three parameters (see Fig. A.1, Table A.1). Two come from the fitting of the EMD with a straight line: the slope of this line and the difference between the minimum EM (at  $T_{\min}$ ) and the local maximum at  $\log T$  [K] =  $6.2 - 6.4$  ( $\Delta EM_1$ ). The fit makes use of values in the temperature range  $\log T$  [K] =  $4.2 - T_{\min}$ . Since the groups 1 and 2 have only 4 objects in total we applied only one fit to all of them.

We need also a way to account for the different sampling of the EMD in  $T$ , from the 0.1 dex binning used in the EMD to the 3-temperature fit typical in low resolution spectra. The fits with 1 or 2 temperature are assumed to be like the 3-T fits with the remaining temperatures considered as negligible. The third parameter needed in our model accounts for this binning, in the form of a vertical shift of the EM ( $\Delta EM_2$ ) to be added to  $\Delta EM_1$ . This parameter shows a dependence on the level of activity, according to the distribution of mass in temperature. We used a representative star for each group, all of them of spectral type K2V:  $\alpha$  Cen B (group 1),  $\epsilon$  Eri (group 2), and AB Dor (group 3). The  $\Delta EM_2$  of each case is listed in Table A.1.

Depending on the temperature and EM found in the targets in our sample we use one of the three groups, and extrapolate the EM of the transition region using the value of EM at the temperature closer to  $\log T$  (K) = 6.3 ( $EM_{6.3}$ ): we first determine the EM of  $T_{\min}$  (using  $\log T_{\min}$  (K) = 5.7):  $EM_{\min} = EM_{\log T \sim 6.3} - \Delta EM_1 - \Delta EM_2$ . Then we extend the EM at lower temperatures with a straight line with the slope in Table A.1, resulting in the values listed in Table A.2. Uncertainties in the lower temperature EMD are calculated based on those from Table A.1.

We made some tests to check the accuracy of the calculation with this method. We used the same three representative stars ( $\alpha$  Cen B,  $\epsilon$  Eri, and AB Dor) with a complete EMD calculated using UV lines, and compared to the flux in same spectral ranges using 3-T model combined with the extrapolated EM at lower temperatures. The values measured from both models (Table A.3) are very similar, so we are confident that the approach followed is correct.

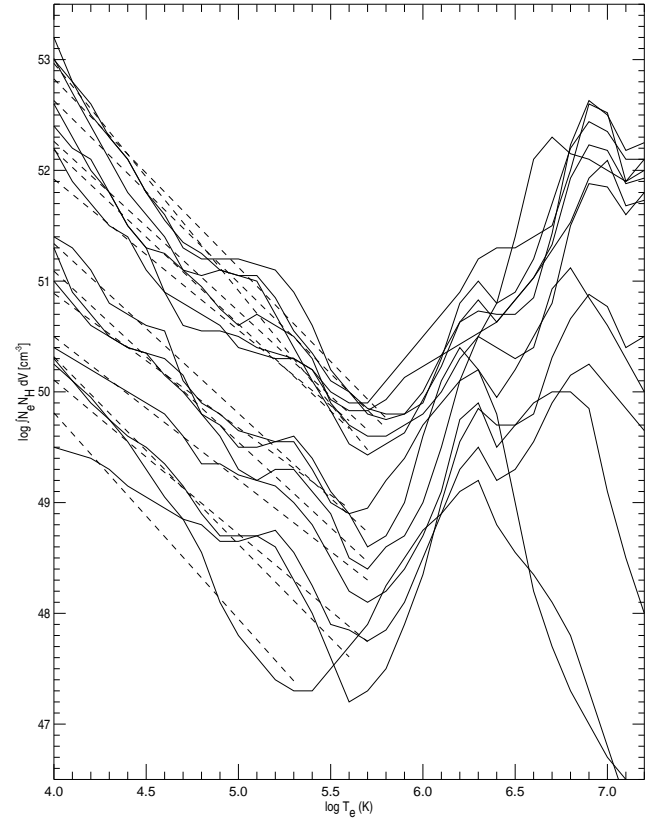


**Fig. A.1.** Linear fits (dashed lines) applied to the cool side of the EMD (solid lines) of well known coronal models.

**Table A.1.** Transition region EMD. Fit parameters

Activity level	Slope	$\Delta EM_1$ (cm $^{-3}$ )	$\Delta EM_2$ (cm $^{-3}$ )
Low	$-1.66 \pm 0.15$	$1.84 \pm 0.36$	0.6
Medium	$-1.66 \pm 0.15$	$1.84 \pm 0.36$	0.1
High	$-1.53 \pm 0.26$	$1.19 \pm 0.25$	1.8

Finally we compared the calculation of the EUV flux of  $\epsilon$  Eri with the direct EUVE spectrum. The luminosity in the band 80 – 170 Å in the observed spectrum was  $3.2e+27$  erg s $^{-1}$ , in the model based on the whole EMD was  $2.7e+27$ , and in the model based on the 3T+extrapolated EMs we get  $1.9e+27$ . These differences are very small considering the process followed to get the synthetic spectra. We are confident that the method can be safely applied to all late type stars (late F to mid M spectral types).

**Table A.2.** Emission measure distribution in the transition region

Star	EM (cm <sup>-3</sup> ) <sup>a</sup>																	
	log T (K)=4.0	4.1	4.2	4.3	4.4	4.5	4.6	4.7	4.8	4.9	5.0	5.1	5.2	5.3	5.4	5.5	5.6	5.7
14 Her	49.96 <sup>+0.62</sup> <sub>-0.61</sub>	49.80 <sup>+0.60</sup> <sub>-0.60</sub>	49.63 <sup>+0.59</sup> <sub>-0.59</sub>	49.46 <sup>+0.57</sup> <sub>-0.57</sub>	49.30 <sup>+0.55</sup> <sub>-0.55</sub>	49.13 <sup>+0.54</sup> <sub>-0.54</sub>	48.97 <sup>+0.52</sup> <sub>-0.53</sub>	48.80 <sup>+0.51</sup> <sub>-0.51</sub>	48.63 <sup>+0.49</sup> <sub>-0.49</sub>	48.47 <sup>+0.48</sup> <sub>-0.48</sub>	48.30 <sup>+0.47</sup> <sub>-0.46</sub>	48.14 <sup>+0.45</sup> <sub>-0.45</sub>	47.97 <sup>+0.44</sup> <sub>-0.44</sub>	47.80 <sup>+0.42</sup> <sub>-0.42</sub>	47.64 <sup>+0.40</sup> <sub>-0.41</sub>	47.47 <sup>+0.39</sup> <sub>-0.39</sub>	47.31 <sup>+0.37</sup> <sub>-0.38</sub>	47.14 <sup>+0.36</sup> <sub>-0.36</sub>
16 Cyg B	< 50.40	< 50.22	< 50.04	< 49.85	< 49.67	< 49.49	< 49.31	< 49.13	< 48.95	< 48.77	< 48.59	< 48.41	< 48.23	< 48.04	< 47.86	< 47.68	< 47.50	< 47.32
2M 1207 A	< 49.52	< 49.34	< 49.16	< 48.97	< 48.79	< 48.61	< 48.43	< 48.25	< 48.07	< 47.89	< 47.71	< 47.53	< 47.35	< 47.16	< 46.98	< 46.80	< 46.62	< 46.44
30 Ari B	50.66 <sup>+0.69</sup> <sub>-0.69</sub>	50.51 <sup>+0.66</sup> <sub>-0.67</sub>	50.36 <sup>+0.64</sup> <sub>-0.64</sub>	50.20 <sup>+0.62</sup> <sub>-0.61</sub>	50.05 <sup>+0.59</sup> <sub>-0.59</sub>	49.90 <sup>+0.56</sup> <sub>-0.57</sub>	49.74 <sup>+0.54</sup> <sub>-0.53</sub>	49.59 <sup>+0.51</sup> <sub>-0.51</sub>	49.44 <sup>+0.48</sup> <sub>-0.48</sub>	49.28 <sup>+0.46</sup> <sub>-0.45</sub>	49.13 <sup>+0.43</sup> <sub>-0.43</sub>	48.98 <sup>+0.40</sup> <sub>-0.41</sub>	48.83 <sup>+0.38</sup> <sub>-0.38</sub>	48.67 <sup>+0.36</sup> <sub>-0.35</sub>	48.52 <sup>+0.33</sup> <sub>-0.33</sub>	48.37 <sup>+0.30</sup> <sub>-0.31</sub>	48.21 <sup>+0.28</sup> <sub>-0.27</sub>	48.06 <sup>+0.25</sup> <sub>-0.25</sub>
47 UMa	48.61 <sup>+0.62</sup> <sub>-0.61</sub>	48.45 <sup>+0.60</sup> <sub>-0.60</sub>	48.28 <sup>+0.59</sup> <sub>-0.59</sub>	48.11 <sup>+0.57</sup> <sub>-0.57</sub>	47.95 <sup>+0.55</sup> <sub>-0.55</sub>	47.78 <sup>+0.54</sup> <sub>-0.54</sub>	47.62 <sup>+0.53</sup> <sub>-0.53</sub>	47.45 <sup>+0.51</sup> <sub>-0.51</sub>	47.28 <sup>+0.50</sup> <sub>-0.50</sub>	47.12 <sup>+0.48</sup> <sub>-0.48</sub>	46.95 <sup>+0.46</sup> <sub>-0.46</sub>	46.79 <sup>+0.45</sup> <sub>-0.45</sub>	46.62 <sup>+0.43</sup> <sub>-0.43</sub>	46.45 <sup>+0.42</sup> <sub>-0.42</sub>	46.29 <sup>+0.40</sup> <sub>-0.41</sub>	46.12 <sup>+0.39</sup> <sub>-0.39</sub>	45.96 <sup>+0.37</sup> <sub>-0.38</sub>	45.79 <sup>+0.36</sup> <sub>-0.36</sub>
51 Peg	< 50.22	< 50.04	< 49.86	< 49.67	< 49.49	< 49.31	< 49.13	< 48.95	< 48.77	< 48.59	< 48.41	< 48.23	< 48.05	< 47.86	< 47.68	< 47.50	< 47.32	< 47.14
55 Cnc	49.73 <sup>+0.62</sup> <sub>-0.61</sub>	49.57 <sup>+0.60</sup> <sub>-0.60</sub>	49.40 <sup>+0.59</sup> <sub>-0.59</sub>	49.23 <sup>+0.57</sup> <sub>-0.57</sub>	49.07 <sup>+0.55</sup> <sub>-0.55</sub>	48.90 <sup>+0.54</sup> <sub>-0.54</sub>	48.74 <sup>+0.52</sup> <sub>-0.53</sub>	48.57 <sup>+0.51</sup> <sub>-0.51</sub>	48.40 <sup>+0.50</sup> <sub>-0.49</sub>	48.24 <sup>+0.48</sup> <sub>-0.48</sub>	48.07 <sup>+0.47</sup> <sub>-0.46</sub>	47.91 <sup>+0.45</sup> <sub>-0.45</sub>	47.74 <sup>+0.43</sup> <sub>-0.43</sub>	47.57 <sup>+0.42</sup> <sub>-0.42</sub>	47.41 <sup>+0.40</sup> <sub>-0.41</sub>	47.24 <sup>+0.39</sup> <sub>-0.39</sub>	47.08 <sup>+0.37</sup> <sub>-0.38</sub>	46.91 <sup>+0.36</sup> <sub>-0.36</sub>
$\beta$ Pic	49.23 <sup>+0.62</sup> <sub>-0.61</sub>	49.07 <sup>+0.60</sup> <sub>-0.59</sub>	48.90 <sup>+0.59</sup> <sub>-0.59</sub>	48.73 <sup>+0.57</sup> <sub>-0.57</sub>	48.57 <sup>+0.55</sup> <sub>-0.55</sub>	48.40 <sup>+0.54</sup> <sub>-0.54</sub>	48.24 <sup>+0.53</sup> <sub>-0.53</sub>	48.07 <sup>+0.51</sup> <sub>-0.51</sub>	47.90 <sup>+0.50</sup> <sub>-0.49</sub>	47.74 <sup>+0.48</sup> <sub>-0.48</sub>	47.57 <sup>+0.47</sup> <sub>-0.46</sub>	47.41 <sup>+0.45</sup> <sub>-0.45</sub>	47.24 <sup>+0.43</sup> <sub>-0.43</sub>	47.07 <sup>+0.42</sup> <sub>-0.42</sub>	46.91 <sup>+0.40</sup> <sub>-0.41</sub>	46.74 <sup>+0.39</sup> <sub>-0.39</sub>	46.58 <sup>+0.37</sup> <sub>-0.38</sub>	46.41 <sup>+0.36</sup> <sub>-0.36</sub>
GJ 317	49.69 <sup>+0.62</sup> <sub>-0.61</sub>	49.53 <sup>+0.60</sup> <sub>-0.60</sub>	49.36 <sup>+0.58</sup> <sub>-0.58</sub>	49.19 <sup>+0.57</sup> <sub>-0.57</sub>	49.03 <sup>+0.55</sup> <sub>-0.55</sub>	48.86 <sup>+0.54</sup> <sub>-0.54</sub>	48.70 <sup>+0.53</sup> <sub>-0.53</sub>	48.53 <sup>+0.51</sup> <sub>-0.51</sub>	48.36 <sup>+0.50</sup> <sub>-0.49</sub>	48.20 <sup>+0.48</sup> <sub>-0.48</sub>	48.03 <sup>+0.46</sup> <sub>-0.46</sub>	47.87 <sup>+0.45</sup> <sub>-0.45</sub>	47.70 <sup>+0.43</sup> <sub>-0.43</sub>	47.53 <sup>+0.42</sup> <sub>-0.42</sub>	47.37 <sup>+0.40</sup> <sub>-0.41</sub>	47.20 <sup>+0.39</sup> <sub>-0.39</sub>	47.04 <sup>+0.38</sup> <sub>-0.38</sub>	46.87 <sup>+0.36</sup> <sub>-0.36</sub>
GJ 436	49.10 <sup>+0.62</sup> <sub>-0.61</sub>	48.94 <sup>+0.60</sup> <sub>-0.60</sub>	48.77 <sup>+0.59</sup> <sub>-0.59</sub>	48.60 <sup>+0.57</sup> <sub>-0.57</sub>	48.44 <sup>+0.55</sup> <sub>-0.55</sub>	48.27 <sup>+0.54</sup> <sub>-0.54</sub>	48.11 <sup>+0.53</sup> <sub>-0.53</sub>	47.94 <sup>+0.51</sup> <sub>-0.51</sub>	47.77 <sup>+0.50</sup> <sub>-0.49</sub>	47.61 <sup>+0.48</sup> <sub>-0.48</sub>	47.44 <sup>+0.46</sup> <sub>-0.46</sub>	47.28 <sup>+0.45</sup> <sub>-0.45</sub>	47.11 <sup>+0.44</sup> <sub>-0.43</sub>	46.94 <sup>+0.42</sup> <sub>-0.42</sub>	46.78 <sup>+0.40</sup> <sub>-0.41</sub>	46.61 <sup>+0.39</sup> <sub>-0.39</sub>	46.45 <sup>+0.37</sup> <sub>-0.38</sub>	46.28 <sup>+0.36</sup> <sub>-0.36</sub>
GJ 674	50.05 <sup>+0.69</sup> <sub>-0.69</sub>	49.90 <sup>+0.66</sup> <sub>-0.67</sub>	49.75 <sup>+0.64</sup> <sub>-0.65</sub>	49.59 <sup>+0.62</sup> <sub>-0.61</sub>	49.44 <sup>+0.59</sup> <sub>-0.59</sub>	49.29 <sup>+0.56</sup> <sub>-0.57</sub>	49.13 <sup>+0.54</sup> <sub>-0.53</sub>	48.98 <sup>+0.51</sup> <sub>-0.51</sub>	48.83 <sup>+0.48</sup> <sub>-0.48</sub>	48.67 <sup>+0.46</sup> <sub>-0.45</sub>	48.52 <sup>+0.43</sup> <sub>-0.43</sub>	48.37 <sup>+0.40</sup> <sub>-0.41</sub>	48.22 <sup>+0.38</sup> <sub>-0.39</sub>	48.06 <sup>+0.36</sup> <sub>-0.35</sub>	47.91 <sup>+0.33</sup> <sub>-0.33</sub>	47.76 <sup>+0.30</sup> <sub>-0.31</sub>	47.60 <sup>+0.28</sup> <sub>-0.27</sub>	47.45 <sup>+0.25</sup> <sub>-0.25</sub>
GJ 86	< 51.56	< 51.38	< 51.20	< 51.01	< 50.83	< 50.65	< 50.47	< 50.29	< 50.11	< 49.93	< 49.75	< 49.57	< 49.39	< 49.20	< 49.02	< 48.84	< 48.66	< 48.48
GJ 876	48.81 <sup>+0.62</sup> <sub>-0.61</sub>	48.65 <sup>+0.60</sup> <sub>-0.60</sub>	48.48 <sup>+0.59</sup> <sub>-0.59</sub>	48.31 <sup>+0.57</sup> <sub>-0.57</sub>	48.15 <sup>+0.55</sup> <sub>-0.55</sub>	47.98 <sup>+0.54</sup> <sub>-0.54</sub>	47.82 <sup>+0.52</sup> <sub>-0.53</sub>	47.65 <sup>+0.51</sup> <sub>-0.51</sub>	47.48 <sup>+0.50</sup> <sub>-0.49</sub>	47.32 <sup>+0.48</sup> <sub>-0.48</sub>	47.15 <sup>+0.47</sup> <sub>-0.46</sub>	46.99 <sup>+0.45</sup> <sub>-0.45</sub>	46.82 <sup>+0.44</sup> <sub>-0.44</sub>	46.65 <sup>+0.42</sup> <sub>-0.43</sub>	46.49 <sup>+0.40</sup> <sub>-0.41</sub>	46.32 <sup>+0.39</sup> <sub>-0.39</sub>	46.16 <sup>+0.37</sup> <sub>-0.38</sub>	45.99 <sup>+0.36</sup> <sub>-0.36</sub>
GQ Lup	53.31 <sup>+0.62</sup> <sub>-0.61</sub>	53.15 <sup>+0.60</sup> <sub>-0.60</sub>	52.98 <sup>+0.58</sup> <sub>-0.58</sub>	52.81 <sup>+0.57</sup> <sub>-0.57</sub>	52.65 <sup>+0.55</sup> <sub>-0.55</sub>	52.48 <sup>+0.54</sup> <sub>-0.54</sub>	52.32 <sup>+0.53</sup> <sub>-0.53</sub>	52.15 <sup>+0.51</sup> <sub>-0.51</sub>	51.98 <sup>+0.50</sup> <sub>-0.49</sub>	51.82 <sup>+0.48</sup> <sub>-0.48</sub>	51.65 <sup>+0.47</sup> <sub>-0.46</sub>	51.49 <sup>+0.45</sup> <sub>-0.45</sub>	51.32 <sup>+0.43</sup> <sub>-0.43</sub>	51.15 <sup>+0.42</sup> <sub>-0.42</sub>	50.99 <sup>+0.40</sup> <sub>-0.41</sub>	50.82 <sup>+0.39</sup> <sub>-0.39</sub>	50.66 <sup>+0.37</sup> <sub>-0.38</sub>	50.49 <sup>+0.36</sup> <sub>-0.36</sub>
HD 4308	< 49.64	< 49.46	< 49.28	< 49.09	< 48.91	< 48.73	< 48.55	< 48.37	< 48.19	< 48.01	< 47.83	< 47.65	< 47.47	< 47.28	< 47.10	< 46.92	< 46.74	< 46.56
HD 20367	51.59 <sup>+0.62</sup> <sub>-0.61</sub>	51.43 <sup>+0.60</sup> <sub>-0.60</sub>	51.26 <sup>+0.59</sup> <sub>-0.59</sub>	51.09 <sup>+0.57</sup> <sub>-0.57</sub>	50.93 <sup>+0.55</sup> <sub>-0.55</sub>	50.76 <sup>+0.54</sup> <sub>-0.54</sub>	50.60 <sup>+0.52</sup> <sub>-0.53</sub>	50.43 <sup>+0.51</sup> <sub>-0.51</sub>	50.26 <sup>+0.50</sup> <sub>-0.49</sub>	50.10 <sup>+0.48</sup> <sub>-0.48</sub>	49.93 <sup>+0.47</sup> <sub>-0.46</sub>	49.77 <sup>+0.45</sup> <sub>-0.45</sub>	49.60 <sup>+0.43</sup> <sub>-0.43</sub>	49.43 <sup>+0.42</sup> <sub>-0.42</sub>	49.27 <sup>+0.40</sup> <sub>-0.41</sub>	49.10 <sup>+0.39</sup> <sub>-0.39</sub>	48.94 <sup>+0.37</sup> <sub>-0.38</sub>	48.77 <sup>+0.36</sup> <sub>-0.36</sub>
HD 27442	< 49.83	< 49.65	< 49.47	< 49.28	< 49.10	< 48.92	< 48.74	< 48.56	< 48.38	< 48.20	< 48.02	< 47.84	< 47.66	< 47.47	< 47.29	< 47.11	< 46.93	< 46.75
HD 46375	50.75 <sup>+0.62</sup> <sub>-0.61</sub>	50.59 <sup>+0.60</sup> <sub>-0.60</sub>	50.42 <sup>+0.59</sup> <sub>-0.59</sub>	50.25 <sup>+0.57</sup> <sub>-0.57</sub>	50.09 <sup>+0.55</sup> <sub>-0.55</sub>	49.92 <sup>+0.54</sup> <sub>-0.54</sub>	49.76 <sup>+0.52</sup> <sub>-0.53</sub>	49.59 <sup>+0.51</sup> <sub>-0.51</sub>	49.42 <sup>+0.50</sup> <sub>-0.49</sub>	49.26 <sup>+0.48</sup> <sub>-0.48</sub>	49.09 <sup>+0.47</sup> <sub>-0.46</sub>	48.93 <sup>+0.45</sup> <sub>-0.45</sub>	48.76 <sup>+0.43</sup> <sub>-0.43</sub>	48.59 <sup>+0.42</sup> <sub>-0.42</sub>	48.43 <sup>+0.40</sup> <sub>-0.41</sub>	48.26 <sup>+0.39</sup> <sub>-0.39</sub>	48.10 <sup>+0.37</sup> <sub>-0.38</sub>	47.93 <sup>+0.36</sup> <sub>-0.36</sub>
HD 49674	51.21 <sup>+0.62</sup> <sub>-0.61</sub>	51.05 <sup>+0.60</sup> <sub>-0.60</sub>	50.88 <sup>+0.58</sup> <sub>-0.58</sub>	50.71 <sup>+0.57</sup> <sub>-0.57</sub>	50.55 <sup>+0.55</sup> <sub>-0.55</sub>	50.38 <sup>+0.54</sup> <sub>-0.54</sub>	50.22 <sup>+0.53</sup> <sub>-0.53</sub>	50.05 <sup>+0.51</sup> <sub>-0.51</sub>	49.88 <sup>+0.49</sup> <sub>-0.49</sub>	49.72 <sup>+0.48</sup> <sub>-0.48</sub>	49.55 <sup>+0.46</sup> <sub>-0.46</sub>	49.39 <sup>+0.45</sup> <sub>-0.45</sub>	49.22 <sup>+0.43</sup> <sub>-0.43</sub>	49.05 <sup>+0.42</sup> <sub>-0.42</sub>	48.89 <sup>+0.40</sup> <sub>-0.41</sub>	48.72 <sup>+0.39</sup> <sub>-0.39</sub>	48.56 <sup>+0.37</sup> <sub>-0.38</sub>	48.39 <sup>+0.36</sup> <sub>-0.36</sub>
HD 50554	< 50.02	< 49.84	< 49.66	< 49.47	< 49.29	< 49.11	< 48.93	< 48.75	< 48.57	< 48.39	< 48.21	< 48.03	< 47.85	< 47.66	< 47.48	< 47.30	< 47.12	< 46.94
HD 52265	49.84 <sup>+0.62</sup> <sub>-0.61</sub>	49.68 <sup>+0.60</sup> <sub>-0.60</sub>	49.51 <sup>+0.59</sup> <sub>-0.59</sub>	49.34 <sup>+0.57</sup> <sub>-0.57</sub>	49.18 <sup>+0.55</sup> <sub>-0.55</sub>	49.01 <sup>+0.54</sup> <sub>-0.54</sub>	48.85 <sup>+0.52</sup> <sub>-0.53</sub>	48.68 <sup>+0.51</sup> <sub>-0.51</sub>	48.51 <sup>+0.50</sup> <sub>-0.49</sub>	48.35 <sup>+0.48</sup> <sub>-0.48</sub>	48.18 <sup>+0.47</sup> <sub>-0.46</sub>	48.02 <sup>+0.45</sup> <sub>-0.45</sub>	47.85 <sup>+0.43</sup> <sub>-0.43</sub>	47.68 <sup>+0.42</sup> <sub>-0.42</sub>	47.52 <sup>+0.40</sup> <sub>-0.41</sub>	47.35 <sup>+0.39</sup> <sub>-0.39</sub>	47.19 <sup>+0.37</sup> <sub>-0.38</sub>	47.02 <sup>+0.36</sup> <sub>-0.36</sub>
HD 70642	49.96 <sup>+0.62</sup> <sub>-0.61</sub>	49.80 <sup>+0.60</sup> <sub>-0.60</sub>	49.63 <sup>+0.58</sup> <sub>-0.58</sub>	49.46 <sup>+0.57</sup> <sub>-0.57</sub>	49.30 <sup>+0.55</sup> <sub>-0.55</sub>	49.13 <sup>+0.54</sup> <sub>-0.54</sub>	48.97 <sup>+0.53</sup> <sub>-0.53</sub>	48.80 <sup>+0.51</sup> <sub>-0.51</sub>	48.63 <sup>+0.49</sup> <sub>-0.49</sub>	48.47 <sup>+0.48</sup> <sub>-0.48</sub>	48.30 <sup>+0.46</sup> <sub>-0.46</sub>	48.14 <sup>+0.45</sup> <sub>-0.45</sub>	47.97 <sup>+0.43</sup> <sub>-0.43</sub>	47.80 <sup>+0.42</sup> <sub>-0.42</sub>	47.64 <sup>+0.40</sup> <sub>-0.41</sub>	47.47 <sup>+0.39</sup> <sub>-0.39</sub>	47.31 <sup>+0.37</sup> <sub>-0.38</sub>	47.14 <sup>+0.36</sup> <sub>-0.36</sub>
HD 75289	< 49.60	< 49.42	< 49.24	< 49.05	< 48.87	< 48.69	< 48.51	< 48.33	< 48.15	< 47.97	< 47.79	< 47.61	< 47.42	< 47.24	< 47.06	< 46.88	< 46.70	< 46.52
HD 93083	50.62 <sup>+0.62</sup> <sub>-0.61</sub>	50.46 <sup>+0.60</sup> <sub>-0.60</sub>	50.29 <sup>+0.59</sup> <sub>-0.59</sub>	50.12 <sup>+0.57</sup> <sub>-0.57</sub>	49.96 <sup>+0.55</sup> <sub>-0.55</sub>	49.79 <sup>+0.54</sup> <sub>-0.54</sub>	49.63 <sup>+0.52</sup> <sub>-0.53</sub>	49.46 <sup>+0.51</sup> <sub>-0.51</sub>	49.29 <sup>+0.50</sup> <sub>-0.49</sub>	49.13 <sup>+0.48</sup> <sub>-0.48</sub>	48.96 <sup>+0.47</sup> <sub>-0.46</sub>	48.80 <sup>+0.45</sup> <sub>-0.45</sub>	48.63 <sup>+0.44</sup> <sub>-0.44</sub>	48.46 <sup>+0.42</sup> <sub>-0.43</sub>	48.30 <sup>+0.40</sup> <sub>-0.41</sub>	48.13 <sup>+0.39</sup> <sub>-0.39</sub>	47.97 <sup>+0.37</sup> <sub>-0.38</sub>	47.80 <sup>+0.36</sup> <sub>-0.36</sub>
HD 95089	< 50.79	< 50.61	< 50.43	< 50.24	< 50.06	< 49.88	< 49.70	< 49.52	< 49.34	< 49.16	< 48.98	< 48.80	< 48.62	< 48.43	< 48.25	< 48.07	< 47.89	< 47.71
HD 99492	50.11 <sup>+0.62</sup> <sub>-0.61</sub>	49.95 <sup>+0.60</sup> <sub>-0.60</sub>	49.78 <sup>+0.59</sup> <sub>-0.59</sub>	49.61 <sup>+0.57</sup> <sub>-0.57</sub>	49.45 <sup>+0.55</sup> <sub>-0.55</sub>	49.28 <sup>+0.54</sup> <sub>-0.54</sub>	49.12 <sup>+0.52</sup> <sub>-0.53</sub>	48.95 <sup>+0.51</sup> <sub>-0.51</sub>	48.78 <sup>+0.50</sup> <sub>-0.49</sub>	48.62 <sup>+0.48</sup> <sub>-0.48</sub>	48.45 <sup>+0.47</sup> <sub>-0.46</sub>	48.29 <sup>+0.45</sup> <sub>-0.45</sub>	48.12 <sup>+0.44</sup> <sub>-0.43</sub>	47.95 <sup>+0.42</sup> <sub>-0.42</sub>	47.79 <sup>+0.40</sup> <sub>-0.41</sub>	47.62 <sup>+0.39</sup> <sub>-0.39</sub>	47.46 <sup>+0.37</sup> <sub>-0.38</sub>	47.29 <sup>+0.36</sup> <sub>-0.36</sub>
HD 101930	49.13 <sup>+0.62</sup> <sub>-0.61</sub>	48.97 <sup>+0.60</sup> <sub>-0.60</sub>	48.80 <sup>+0.58</sup> <sub>-0.58</sub>	48.63 <sup>+0.57</sup> <sub>-0.57</sub>	48.47 <sup>+0.55</sup> <sub>-0.55</sub>	48.30 <sup>+0.54</sup> <sub>-0.54</sub>	48.14 <sup>+0.53</sup> <sub>-0.53</sub>	47.97 <sup>+0.51</sup> <sub>-0.51</sub>	47.80 <sup>+0.49</sup> <sub>-0.49</sub>	47.64 <sup>+0.48</sup> <sub>-0.48</sub>	47.47 <sup>+0.46</sup> <sub>-0.46</sub>	47.31 <sup>+0.45</sup> <sub>-0.45</sub>	47.14 <sup>+0.43</sup> <sub>-0.43</sub>	46.97 <sup>+0.42</sup> <sub>-0.42</sub>	46.81 <sup>+0.40</sup> <sub>-0.41</sub>	46.64 <sup>+0.39</sup> <sub>-0.39</sub>	46.48 <sup>+0.37</sup> <sub>-0.38</sub>	46.31 <sup>+0.36</sup> <sub>-0.36</sub>
HD 102195	51.92 <sup>+0.62</sup> <sub>-0.61</sub>	51.76 <sup>+0.60</sup> <sub>-0.60</sub>	51.59 <sup>+0.58</sup> <sub>-0.58</sub>	51.42 <sup>+0.57</sup> <sub>-0.57</sub>	51.26 <sup>+0.55</sup> <sub>-0.55</sub>	51.09 <sup>+0.54</sup> <sub>-0.54</sub>	50.93 <sup>+0.53</sup> <sub>-0.53</sub>	50.76 <sup>+0.51</sup> <sub>-0.51</sub>	50.59 <sup>+0.50</sup> <sub>-0.49</sub>									

**Table A.3.** Comparison of fluxes depending on models used<sup>a</sup>

Range (Å)	$L$ (erg s <sup>-1</sup> )					
	$\alpha$ Cen B		$\epsilon$ Eri		AB Dor	
	EMD	3T	EMD	3T	EMD	3T
5 – 100	7.0e+26	9.3e+26	1.8e+28	1.6e+28	2.1e+30	1.6e+30
100 – 920	6.8e+27	4.1e+27	2.7e+28	1.7e+28	6.3e+29	4.2e+29

**Notes.** <sup>(a)</sup> The “3T” model includes also the predicted EM values in the transition region

**Table B.1.** XMM/RGS line fluxes of  $\alpha$  Cen B<sup>a</sup>

Ion	$\lambda_{\text{model}}$	$\log T_{\text{max}}$	$F_{\text{obs}}$	S/N	ratio	Blends
Ne ix	13.4473	6.6	9.59e-15	5.6	-0.10	Fe xix 13.4970, 13.5180, Ne ix 13.5531
Ne ix	13.6990	6.6	1.30e-14	5.3	0.08	Ni xix 13.7790, Fe xvii 13.8250
Fe xvii	15.0140	6.7	6.62e-14	10.7	-0.03	
Fe xvii	15.2610	6.7	4.29e-14	8.1	0.20	O viii 15.1760, Fe xvii 15.2509, 15.2615
O viii	16.0055	6.5	1.23e-14	4.0	-0.02	Fe xvii 15.9956, Fe xviii 16.0040, O viii 16.0067
Fe xvii	16.7800	6.7	1.38e-14	3.9	-0.35	
Fe xvii	17.0510	6.7	6.35e-14	9.8	-0.04	Fe xvii 17.0960
O vii	18.6270	6.3	1.16e-14	3.1	-0.10	
O viii	18.9671	6.5	7.65e-14	10.6	0.00	O viii 18.9725
O vii	21.6015	6.3	1.29e-13	20.2	0.02	
O vii	22.0977	6.3	1.22e-13	12.5	0.19	
N vii	24.7792	6.3	3.68e-14	11.1	-0.04	N vii 24.7846
Ca xi	25.3520	6.3	7.10e-15	3.0	0.28	N vii 25.4030
C vi	28.4652	6.2	1.32e-14	3.3	-0.27	Ar xv 28.3860, C vi 28.4663
N vi	28.7870	6.2	2.54e-14	5.0	-0.08	
N vi	29.5347	6.1	2.69e-14	5.5	0.13	
Ca xi	30.4710	6.3	2.51e-14	4.7	-0.14	S xiv 30.4270, 30.4690
C vi	33.7342	6.1	1.83e-13	12.4	0.01	C vi 33.7396
C v	34.9728	6.0	1.49e-14	3.2	0.03	Ar ix 35.0240
Ca xi	35.2750	6.3	1.87e-14	3.6	0.16	S xii 35.2750
S xiii	35.6670	6.4	3.93e-14	5.6	-0.01	Ca xi 35.6340, 35.7370

**Notes.** <sup>(a)</sup> Line fluxes in erg cm<sup>-2</sup> s<sup>-1</sup>.  $\lambda_{\text{model}}$  (Å) is the APED model wavelength corresponding to the measured line.  $\log T_{\text{max}}$  indicates the maximum temperature (K) of formation of the line (unweighted by the EMD). “Ratio” is the  $\log(F_{\text{obs}}/F_{\text{pred}})$  of the line. Blends amounting to more than 5% of the total flux for each line are indicated.

## Appendix B: Emission Measure Distribution of $\alpha$ Cen B

We have calculated the Emission Measure Distribution (EMD) of the K2V star  $\alpha$  Cen B, needed to test the extrapolation of the lower EMD temperature and the synthesis of the EUV spectra. We use the UV lines fluxes measured by Sanz-Forcada et al. (2003a), and the XMM-Newton/RGS lines fluxes listed in Table B.1, from an observation taken on Jan 2009 (Fig. B.1). The coronal model (the EMD) was constructed following Sanz-Forcada et al. (2003b). The resulting EMD (Table B.2) is displayed in Fig. B.2, with coronal abundances as listed in Table B.3. A global fit to the Chandra/LETG spectrum was applied by Raassen et al. (2003), with similar results in the corona.

## Appendix C: The X-Exoplanets Data Server

The X-Exoplanets data server<sup>2</sup> provides information on the planet-bearing stars that have been observed with XMM-Newton or Chandra. In the near future, synthetic spectra covering the EUV range (Sanz-Forcada et al., 2010a) and EUVE data will also be available. The system contains reduced, science-ready

<sup>2</sup> <http://sdc.cab.inta-csic.es/xexoplanets/>

**Table B.2.** Emission measure distribution of  $\alpha$  Cen B

$\log T$ (K)	EM (cm <sup>-3</sup> ) <sup>a</sup>
4.0	49.53:
4.1	49.48:
4.2	49.43:
4.3	49.33 <sup>+0.20</sup> <sub>-0.30</sub>
4.4	49.18 <sup>+0.10</sup> <sub>-0.20</sub>
4.5	49.08 <sup>+0.10</sup> <sub>-0.20</sub>
4.6	48.98 <sup>+0.20</sup> <sub>-0.30</sub>
4.7	48.88 <sup>+0.10</sup> <sub>-0.30</sub>
4.8	48.58 <sup>+0.20</sup> <sub>-0.20</sub>
4.9	48.13 <sup>+0.10</sup> <sub>-0.10</sub>
5.0	47.83 <sup>+0.10</sup> <sub>-0.30</sub>
5.1	47.63 <sup>+0.20</sup> <sub>-0.30</sub>
5.2	47.43:
5.3	47.33:
5.4	47.33:
5.5	47.53:
5.6	47.73:
5.7	47.93:
5.8	48.28 <sup>+0.40</sup> <sub>-0.30</sub>
5.9	48.53 <sup>+0.40</sup> <sub>-0.30</sub>
6.0	48.78 <sup>+0.20</sup> <sub>-0.30</sub>
6.1	48.93 <sup>+0.10</sup> <sub>-0.40</sub>
6.2	49.13 <sup>+0.20</sup> <sub>-0.20</sub>
6.3	49.23 <sup>+0.10</sup> <sub>-0.20</sub>
6.4	48.83 <sup>+0.10</sup> <sub>-0.20</sub>
6.5	48.58 <sup>+0.20</sup> <sub>-0.30</sub>
6.6	48.38 <sup>+0.20</sup> <sub>-0.20</sub>
6.7	48.13 <sup>+0.20</sup> <sub>-0.40</sub>
6.8	47.83 <sup>+0.10</sup> <sub>-0.30</sub>
6.9	47.33:
7.0	46.83:

**Notes.** <sup>(a)</sup> Emission measure (EM= $\log \int N_e N_H dV$ ), where  $N_e$  and  $N_H$  are electron and hydrogen densities, in cm<sup>-3</sup>. Error bars provided are not independent between the different temperatures, as explained in Sanz-Forcada et al. (2003a)

**Table B.3.** Coronal abundances of  $\alpha$  Cen B (solar units<sup>a</sup>).

X	FIP (eV)	Ref. <sup>a</sup>	(AG89 <sup>a</sup> )	[X/H]
C	11.26	8.39	(8.56)	0.04± 0.11
N	14.53	7.78	(8.05)	-0.01± 0.14
O	13.61	8.66	(8.93)	-0.40± 0.12
Ne	21.56	7.84	(8.09)	-0.48± 0.19
Si	8.15	7.51	(7.55)	-0.44± 0.10
S	10.36	7.14	(7.21)	0.49± 0.18
Ca	6.11	6.31	(6.36)	0.22± 0.27
Fe	7.87	7.45	(7.67)	0.19± 0.19

**Notes.** <sup>(a)</sup> Solar photospheric abundances from Asplund et al. (2005), adopted in this table, are expressed in logarithmic scale. Note that several values have been updated in the literature since Anders & Grevesse (1989, AG89), also listed in parenthesis for easier comparison.

data and was set up to facilitate analysis of the effects of coronal radiation on exoplanets atmospheres.

### C.1. Functionalities: Search

The X-Exoplanets data server is accessed by means of a web-based fill-in form that permits queries by list of objects and coordinates and radius. Searches can be customized to include physical parameters of the stars and planets as well as light curves and reduced spectra obtained from XMM-Newton and Chandra data.

### C.2. Functionalities: Results

An example of the result of a query is given in Fig. C.1. Light curves and reduced spectra can be visualized by clicking on the corresponding link (Fig. C.2). The system incorporates multidownload and preview capabilities. Links to SIMBAD and the Extrasolar Planet Encyclopaedia are also provided.

### C.3. The Virtual Observatory service

VO-compliance of an astronomical archive constitutes an added value of enormous importance for the optimum scientific exploitation of their datasets. The X-Exoplanet service has been designed following the IVOA standards and requirements. In particular, it implements the SSA (Simple Spectral Access) protocol and its associated data model, a standard defined for retrieving 1-D data.

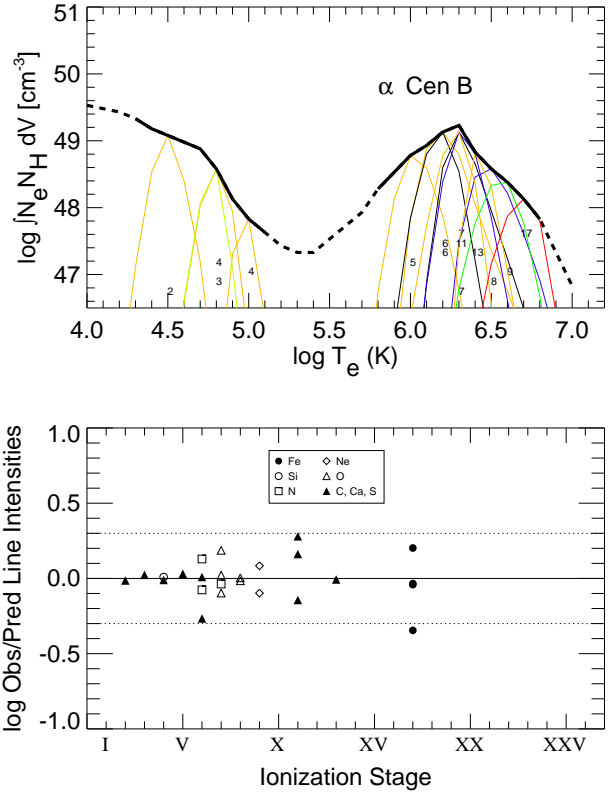


**Fig. B.2.** Upper panel: Emission Measure Distribution of  $\alpha$  Cen B. Thin lines represent the relative contribution function for each ion (the emissivity function multiplied by the EMD at each point). Small numbers indicate the ionization stages of the species. Lower panel indicates the observed-to-predicted line flux ratios for the ion stages in the upper figure. The dotted lines denote a factor of 2.

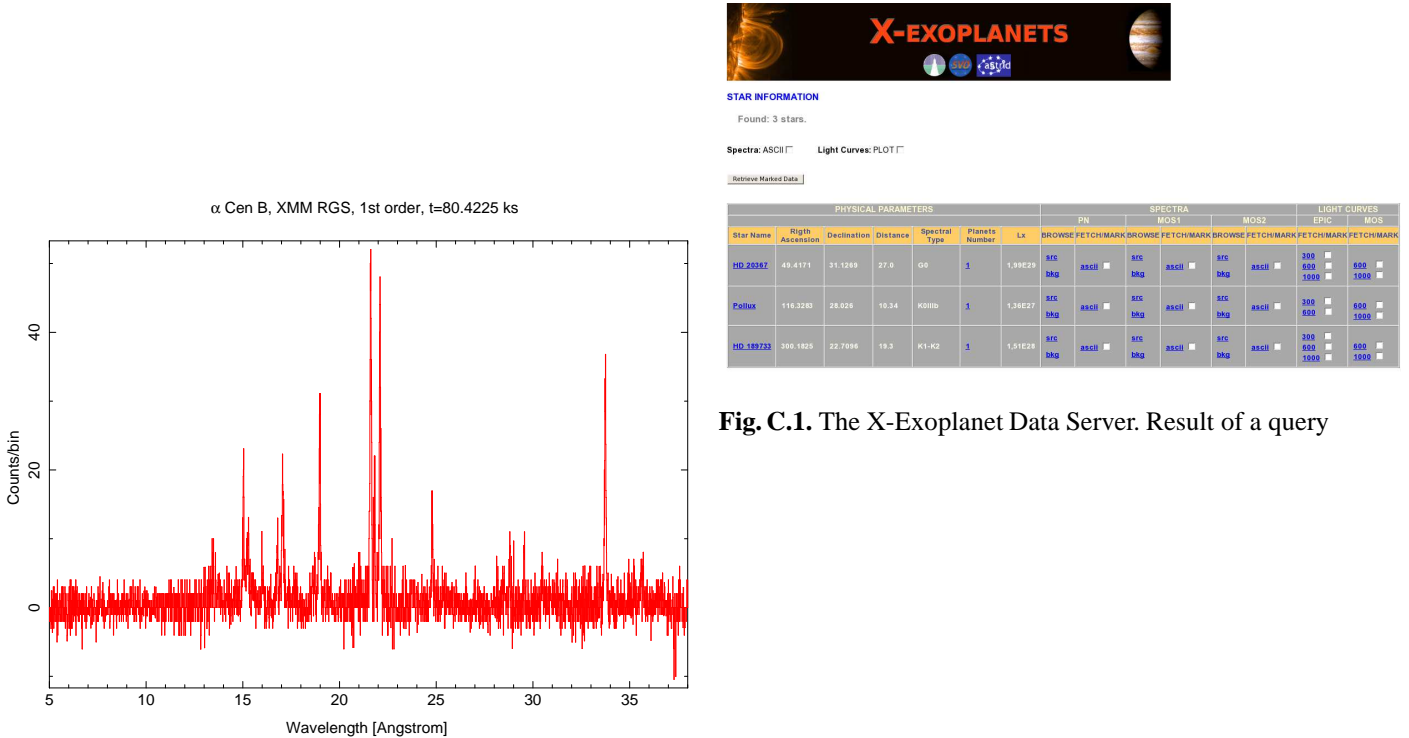


**Fig. B.1.** XMM-Newton RGS combined spectrum of  $\alpha$  Cen B

**Fig. C.1.** The X-Exoplanet Data Server. Result of a query

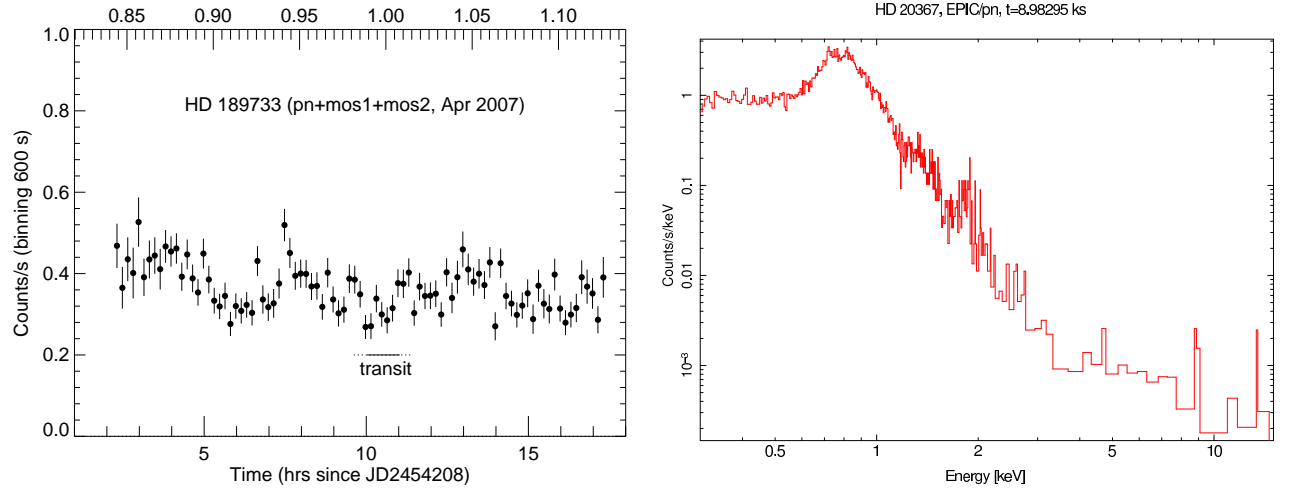


**Fig. C.2.** The X-Exoplanet Data Server. Light curve (left) and reduced spectrum (right). In the light curve of HD 189733 we mark the orbital phase (Winn et al., 2007) of HD 189733 b in the upper axis, as well as the interval when the transit takes place (partial in dotted line, total in solid line).

**Table 3.** X-ray flux (0.12 – 2.48 keV) and fits of stars with exoplanets (XMM-Newton and Chandra data)

Star name	$\log f_X$ ( $\text{erg s}^{-1}\text{cm}^{-2}$ )	$\log T$ (K)	$\log EM$ ( $\text{cm}^{-3}$ )	Elements (X)	[X/H] (Solar values of Anders & Grevesse, 1989)
14 Her	-13.67	$6.49^{+0.06}_{-0.06}$	$49.58^{+0.10}_{-0.10}$	Fe	$-0.22^{+0.00}_{-0.00}$
16 Cyg B	< -14.04	6.30	$49.40^{+0.14}_{-0.14}$	Fe	-0.20
2M1207 A	< -15.27	6.30	$48.52^{+0.34}_{-0.34}$	Fe	-0.20
30 Ari B	-11.74	$6.66^{+0.01}_{-0.01}$ , $6.30^{+0.08}_{-0.08}$ , $6.91^{+0.01}_{-0.01}$	$52.02^{+0.03}_{-0.03}$ , $51.05^{+0.17}_{-0.17}$ , $51.61^{+0.03}_{-0.03}$	Fe, O, Ne	$-0.01^{+0.02}_{-0.02}$ , $-0.48^{+0.04}_{-0.04}$ , $-0.17^{+0.06}_{-0.07}$
47 UMa	-14.92	$6.20^{+0.16}_{-0.20}$	$48.23^{+0.13}_{-0.13}$	Fe	$-0.10^{+0.00}_{-0.20}$
51 Peg	< -13.93	6.30	$49.22^{+0.24}_{-0.24}$	Fe	-0.20
55 Cnc	-13.62	$6.65^{+0.05}_{-0.09}$	$49.35^{+0.06}_{-0.11}$	Fe	$-0.30^{+0.20}_{-0.00}$
$\beta$ Pic	-15.01	$6.29^{+0.10}_{-0.10}$	$48.35^{+0.19}_{-0.19}$	Fe	$-0.30^{+0.20}_{-0.20}$
$\epsilon$ Eri	-10.89	$6.60^{+0.01}_{-0.01}$ , $6.27^{+0.05}_{-0.05}$ , $6.87^{+0.02}_{-0.02}$	$50.67^{+0.05}_{-0.08}$ , $50.29^{+0.07}_{-0.09}$ , $50.22^{+0.07}_{-0.08}$	Fe, O, N, Ne, C	$-0.17^{+0.03}_{-0.02}$ , $-0.25^{+0.07}_{-0.05}$ , $0.30^{+0.09}_{-0.07}$ , $-0.14^{+0.05}_{-0.04}$ , $0.25^{+0.17}_{-0.15}$
GJ 317	-13.86	$6.62^{+0.09}_{-0.09}$	$48.81^{+0.17}_{-0.17}$	Fe	$-0.23^{+0.00}_{-0.44}$
GJ 436	-14.13	$6.76^{+0.15}_{-0.13}$ , $6.26^{+0.19}_{-0.20}$	$48.59^{+0.17}_{-0.32}$ , $48.22^{+0.22}_{-0.55}$	Fe	$-0.74^{+0.45}_{-0.69}$
GJ 674	-11.67	$6.88^{+0.08}_{-0.05}$ , $6.48^{+0.01}_{-0.01}$ , $7.13^{+0.05}_{-0.02}$	$49.62^{+0.12}_{-0.15}$ , $50.44^{+0.03}_{-0.03}$ , $49.71^{+0.04}_{-0.14}$	Fe, O, Ne	$-0.27^{+0.05}_{-0.05}$ , $-0.51^{+0.03}_{-0.03}$ , $-0.13^{+0.07}_{-0.07}$
GJ 86	< -12.74	$6.54^{+0.02}_{-0.02}$	$50.06^{+0.03}_{-0.03}$	Fe	$-0.05^{+0.11}_{-0.11}$
GJ 876	-13.26	$6.65^{+0.02}_{-0.02}$ , $6.18^{+0.00}_{-0.00}$	$48.84^{+0.02}_{-0.03}$ , $47.93^{+0.18}_{-0.33}$	Fe	$-0.37^{+0.06}_{-0.07}$
GQ Lup	-12.92	$6.89^{+0.06}_{-0.07}$ , $7.60^{+0.06}_{-0.07}$	$52.43^{+0.06}_{-0.24}$ , $52.71^{+0.09}_{-0.06}$	Fe	$-0.30^{+0.09}_{-0.00}$
HD 4308	< -14.82	6.30	$48.64^{+0.28}_{-0.11}$	Fe	-0.20
HD 20367	-11.65	$6.30^{+0.99}_{-0.11}$ , $6.65^{+0.12}_{-0.21}$ , $6.95^{+0.03}_{-0.02}$	$50.71^{+0.98}_{-0.44}$ , $51.79^{+0.05}_{-0.60}$ , $51.39^{+0.05}_{-0.07}$	Fe, O, N, Ne	$-0.01^{+0.04}_{-0.05}$ , $-0.36^{+0.10}_{-0.07}$ , $0.19^{+0.18}_{-0.20}$ , $-0.47^{+0.21}_{-0.40}$
HD 27442	< -14.46	6.30	$48.83^{+0.24}_{-0.24}$	Fe	-0.20
HD 46375	-13.96	$6.63^{+0.12}_{-0.10}$	$49.87^{+0.09}_{-0.17}$	Fe	$-0.30^{+0.00}_{-0.00}$
HD 49674	-13.89	$6.49^{+0.18}_{-0.15}$ , $6.00^{+0.00}_{-0.00}$	$50.13^{+0.11}_{-0.97}$ , $50.83^{+0.00}_{-0.00}$	Fe, O	$0.41^{+0.37}_{-0.55}$ , $-0.41^{+0.19}_{-0.86}$
HD 50554	< -14.74	6.30	$49.02^{+0.22}_{-0.46}$	Fe	-0.20
HD 52265	-14.08	$6.43^{+0.12}_{-0.07}$	$49.46^{+0.26}_{-0.33}$	Fe	$0.27^{+0.51}_{-N/A}$
HD 70642	-14.61	$6.53^{+0.21}_{-0.12}$	$49.08^{+0.16}_{-0.29}$	Fe	$-0.30^{+0.20}_{-0.00}$
HD 75289	< -15.10	6.30	$48.60^{+0.34}_{-N/A}$	Fe	-0.20
HD 93083	-14.10	$6.77^{+0.17}_{-0.22}$	$49.74^{+0.15}_{-0.26}$	Fe	$-1.12^{+0.98}_{-N/A}$
HD 95089	< -15.18	6.30	$47.94^{+0.31}_{-N/A}$	Fe	-0.20
HD 99492	-14.04	$6.59^{+0.10}_{-0.07}$	$49.23^{+0.12}_{-0.41}$	Fe	$-0.22^{+0.42}_{-0.59}$
HD 101930	-14.99	6.30	$48.75^{+0.41}_{-N/A}$	Fe	-0.20
HD 102195	-12.57	$6.74^{+0.02}_{-0.02}$ , $6.01^{+0.04}_{-0.01}$	$50.80^{+0.04}_{-0.05}$ , $51.04^{+0.08}_{-0.14}$	Fe	$-0.05^{+0.07}_{-0.06}$
HD 108147	-13.86	$6.60^{+0.16}_{-0.13}$	$50.05^{+0.15}_{-0.26}$	Fe	$-0.10^{+0.00}_{-0.00}$
HD 111232	< -14.65	6.30	$49.05^{+0.06}_{-0.06}$	Fe	-0.20
HD 114386	-14.44	$6.39^{+0.20}_{-0.22}$	$49.20^{+0.20}_{-0.39}$	Fe	$-0.30^{+0.20}_{-0.00}$
HD 114762	< -14.78	6.30	$49.19^{+0.33}_{-N/A}$	Fe	-0.20
HD 114783	< -14.16	$6.38^{+0.12}_{-0.09}$	$49.21^{+0.17}_{-0.33}$	Fe	$-0.30^{+0.20}_{-0.00}$
HD 130322	-13.78	$6.56^{+0.08}_{-0.08}$	$49.94^{+0.10}_{-0.14}$	Fe	$-0.24^{+0.00}_{-0.06}$
HD 154345	-13.47	$6.42^{+0.08}_{-0.05}$	$49.67^{+0.11}_{-0.14}$	Fe	$0.31^{+0.40}_{-0.78}$
HD 164922	< -15.02	6.30	$48.44^{+0.41}_{-N/A}$	Fe	-0.20
HD 179949	-12.56	$6.06^{+0.05}_{-0.04}$ , $6.72^{+0.01}_{-0.01}$	$50.77^{+0.15}_{-0.17}$ , $50.74^{+0.03}_{-0.04}$	Fe	$0.12^{+0.04}_{-0.04}$
HD 187123	< -14.20	6.30	$49.98^{+0.01}_{-0.09}$	Fe	-0.20
HD 189733	-12.47	$6.85^{+0.01}_{-0.01}$ , $6.13^{+0.01}_{-0.01}$ , $6.68^{+0.04}_{-0.05}$	$50.66^{+0.02}_{-0.05}$ , $50.49^{+0.03}_{-0.04}$ , $50.23^{+0.04}_{-0.14}$	Fe, O, Ne	$-0.40^{+0.00}_{-0.00}$ , $-0.05^{+0.02}_{-0.04}$ , $-0.40^{+0.00}_{-0.00}$
HD 190360	< -14.13	6.30	$49.05^{+0.01}_{-0.00}$	Fe	-0.20
HD 195019	< -14.99	6.30	$48.91^{+0.26}_{-0.74}$	Fe	$0.00^{+0.00}_{-0.00}$
HD 209458	< -15.02	6.30	$49.10^{+0.06}_{-0.06}$	Fe	-0.20
HD 216435	-13.38	$6.58^{+0.04}_{-0.03}$	$50.36^{+0.05}_{-0.06}$	Fe	$-0.00^{+0.00}_{-0.23}$
HD 216437	-14.30	$6.40^{+0.21}_{-0.10}$	$49.28^{+0.06}_{-0.19}$	Fe	$-0.30^{+0.20}_{-0.00}$
HD 217107	< -15.17	6.30	$48.20^{+0.45}_{-N/A}$	Fe	-0.20
HD 218566	-13.99	$6.52^{+0.17}_{-0.16}$	$49.72^{+0.21}_{-0.39}$	Fe	$-0.24^{+0.92}_{-N/A}$
HD 330075	-14.97	$6.60^{+1.30}_{-0.24}$	$49.22^{+0.30}_{-N/A}$	Fe	$-0.30^{+0.20}_{-0.00}$
HR 8799	-13.26	$6.54^{+0.07}_{-0.08}$	$50.75^{+0.11}_{-0.14}$	Fe	$-0.55^{+0.60}_{-N/A}$
$\mu$ Ara	< -14.46	6.30	$48.68^{+0.16}_{-0.28}$	Fe	-0.20
NGC 2423 3	< -14.58	6.30	$56.27^{+1.58}_{-N/A}$	Fe	-0.20
Pollux	-12.97	$6.23^{+0.05}_{-0.12}$ , $6.54^{+0.21}_{-0.43}$	$49.90^{+0.06}_{-0.11}$ , $48.70^{+1.08}_{-1.68}$	Fe, O	$0.43^{+0.35}_{-0.34}$ , $-0.36^{+0.30}_{-0.15}$
$\tau$ Boo	-11.51	$6.62^{+0.01}_{-0.01}$ , $6.30^{+0.04}_{-0.04}$ , $6.92^{+0.01}_{-0.01}$	$51.70^{+0.02}_{-0.02}$ , $50.94^{+0.08}_{-0.05}$ , $50.93^{+0.06}_{-0.04}$	Fe, O, Ne, Mg	$-0.28^{+0.00}_{-0.00}$ , $-0.56^{+0.03}_{-0.02}$ , $-0.51^{+0.05}_{-0.06}$ , $-0.28^{+0.05}_{-0.03}$
$\nu$ And	-12.77	$6.53^{+0.02}_{-0.02}$	$50.09^{+0.03}_{-0.04}$	Si, C, N Fe	$-0.09^{+0.05}_{-0.04}$ , $-0.22^{+0.00}_{-0.00}$ , $-0.37^{+0.00}_{-0.00}$ $0.30^{+0.09}_{-0.09}$



**Table 4.** Stars with exoplanets. XUV luminosity predicted in different bands<sup>a</sup>

Star	Luminosity (erg s <sup>-1</sup> ) in the wavelength ranges indicated (in Å)					
	100–200	200–300	300–400	400–550	550–700	700–920
14 Her	26.01±0.08	26.61±0.15	27.10±0.39	26.63±0.39	27.06±0.44	27.34±0.48
16 Cyg B	<26.32	<27.00	<27.37	<26.89	<27.33	<27.65
2M1207 A	<25.44	<26.12	<26.49	<26.01	<26.45	<26.77
30 Ari B	28.65±0.00	28.90±0.00	28.83±0.05	28.19±0.05	27.92±0.20	28.02±0.35
47 UMa	25.64±0.01	25.88±0.04	25.86±0.31	25.29±0.38	25.74±0.42	26.00±0.48
51 Peg	<26.14	<26.82	<27.19	<26.71	<27.15	<27.47
55 Cnc	25.68±0.09	26.10±0.28	26.84±0.43	26.37±0.42	26.83±0.44	27.11±0.49
β Pic	25.31±0.07	25.91±0.14	26.34±0.43	25.87±0.42	26.33±0.44	26.61±0.49
ε Eri	27.69±0.00	27.96±0.00	27.81±0.00	27.26±0.00	27.31±0.00	27.49±0.00
GJ 86	<26.85	<27.64	<28.50	<28.02	<28.49	<28.81
GJ 317	25.32±0.19	25.95±0.36	26.77±0.45	26.31±0.45	26.79±0.44	27.07±0.49
GJ 436	25.26±0.05	25.66±0.19	26.21±0.42	25.75±0.41	26.21±0.44	26.48±0.48
GJ 674	26.94±0.01	27.37±0.03	27.49±0.24	26.97±0.20	27.02±0.37	27.29±0.46
GJ 876	25.44±0.02	25.65±0.10	26.01±0.34	25.52±0.35	25.93±0.42	26.20±0.48
GQ Lup	29.17±0.11	29.51±0.41	30.38±0.47	29.92±0.45	30.41±0.44	30.69±0.49
HD 4308	<25.56	<26.24	<26.61	<26.13	<26.57	<26.89
HD 20367	28.44±0.01	28.67±0.05	28.90±0.26	28.25±0.26	28.51±0.42	28.81±0.48
HD 27442	<25.75	<26.43	<26.80	<26.32	<26.76	<27.08
HD 46375	26.37±0.18	27.00±0.36	27.83±0.46	27.37±0.45	27.85±0.44	28.13±0.49
HD 49674	29.06±0.00	28.43±0.04	28.61±0.21	27.88±0.32	28.11±0.38	28.41±0.44
HD 50554	<25.94	<26.62	<26.99	<26.51	<26.95	<27.27
HD 52265	26.05±0.08	26.97±0.05	27.11±0.29	26.54±0.36	26.95±0.44	27.22±0.48
HD 70642	25.62±0.17	26.28±0.31	27.05±0.45	26.59±0.44	27.06±0.44	27.34±0.49
HD 75289	<25.52	<26.20	<26.57	<26.09	<26.53	<26.85
HD 93083	26.14±0.19	26.81±0.42	27.69±0.47	27.23±0.45	27.72±0.44	28.00±0.49
HD 95089	<26.71	<27.39	<27.76	<27.28	<27.72	<28.04
HD 99492	25.75±0.18	26.39±0.34	27.20±0.45	26.73±0.44	27.21±0.44	27.49±0.49
HD 101930	25.63±0.03	26.27±0.05	26.32±0.35	25.84±0.36	26.24±0.43	26.52±0.48
HD 102195	28.84±0.01	28.51±0.17	29.09±0.36	28.57±0.41	29.03±0.43	29.31±0.48
HD 108147	26.59±0.19	27.21±0.34	28.02±0.45	27.55±0.44	28.03±0.44	28.31±0.49
HD 111232	<25.97	<26.65	<27.02	<26.54	<26.98	<27.30
HD 114386	25.79±0.05	26.45±0.10	26.73±0.38	26.27±0.37	26.69±0.44	26.96±0.48
HD 114762	<26.11	<26.79	<27.16	<26.68	<27.12	<27.44
HD 114783	<25.90	<26.62	<27.17	<26.69	<27.14	<27.46
HD 130322	26.47±0.18	27.13±0.32	27.91±0.45	27.44±0.44	27.92±0.44	28.20±0.49
HD 154345	26.29±0.08	27.24±0.05	27.34±0.28	26.76±0.36	27.16±0.44	27.43±0.48
HD 164922	<25.36	<26.04	<26.41	<25.93	<26.37	<26.69
HD 179949	28.70±0.01	28.42±0.12	28.83±0.36	28.29±0.42	28.76±0.43	29.04±0.48
HD 187123	<26.90	<27.58	<27.95	<27.47	<27.91	<28.23
HD 189733	27.90±0.00	27.86±0.02	27.84±0.13	27.08±0.19	27.48±0.27	27.60±0.43
HD 190360	<25.97	<26.65	<27.02	<26.54	<26.98	<27.30
HD 195019	<25.92	<26.64	<26.89	<26.40	<26.84	<27.16
HD 209458	<26.02	<26.70	<27.07	<26.59	<27.03	<27.35
HD 216435	26.92±0.19	27.56±0.31	28.34±0.44	27.86±0.44	28.34±0.44	28.62±0.49
HD 216437	25.83±0.06	26.50±0.10	26.81±0.38	26.35±0.37	26.77±0.43	27.04±0.48
HD 217107	<25.12	<25.80	<26.17	<25.69	<26.13	<26.45
HD 218566	26.27±0.17	26.94±0.29	27.69±0.45	27.23±0.44	27.70±0.44	27.98±0.49
HD 330075	25.56±0.09	26.02±0.25	26.71±0.42	26.25±0.41	26.70±0.44	26.98±0.49
HR 8799	27.26±0.16	27.92±0.33	28.71±0.46	28.26±0.44	28.73±0.44	29.01±0.49
μ Ara	<25.60	<26.28	<26.65	<26.17	<26.61	<26.93
NGC 2423 3	<33.19	<33.87	<34.24	<33.76	<34.20	<34.52
Pollux	27.68±0.01	27.98±0.01	27.66±0.23	26.93±0.34	27.18±0.41	27.47±0.48
τ Boo	28.21±0.01	28.47±0.12	28.97±0.37	28.35±0.27	28.50±0.42	28.77±0.49
ν And	26.75±0.20	27.46±0.22	28.10±0.40	27.60±0.44	28.07±0.44	28.35±0.49

**Notes.** <sup>(a)</sup> Only stars with XMM-Newton or Chandra data.